













The Traspenna meteorite: heliocentric orbit, atmospheric trajectory, strewn field, and petrography of a new L5 ordinary chondrite

Manuel Andrade ^{1,2}★, José Á. Docobo ^{1,3,4}, Javier García-Guinea ⁵, Pedro P. Campo ⁶,
Mar Tapia ^{7,8}, Luis Sánchez-Muñoz ⁵, Víctor Villasante-Marcos ⁹, Eloy Peña-Asensio ^{10,11},
Josep M. Trigo-Rodríguez ^{11,12}, Jordi Ibáñez-Insa ¹³, Marc Campeny ¹⁴ and Jordi Llorca ¹⁵

¹CITMAga, E-15782 Santiago de Compostela, Galiza, Spain

²Observatorio Astronómico R. M. Aller (OARMA), Departamento de Matemática Aplicada, Escola Politécnica Superior de Enxeñaría (EPSE), Universidade de Santiago de Compostela (USC), Campus Terra, E-27002 Lugo, Galiza, Spain

³Observatorio Astronómico R. M. Aller (OARMA), Departamento de Matemática Aplicada, Facultade de Matemáticas, Universidade de Santiago de Compostela (USC), Campus Vida, E-15782 Santiago de Compostela, Galiza, Spain

⁴Real Academia de Ciencias de Zaragoza, Facultad de Ciencias, C/ Pedro Cerbuna 12, E-50009 Zaragoza, Spain

⁵Museo Nacional de Ciencias Naturales, C/ José Gutiérrez Abascal 2, E-28006 Madrid, Spain

⁶Observatorio Astronómico R. M. Aller (OARMA), Universidade de Santiago de Compostela (USC), Campus Vida, E-15782 Santiago de Compostela, Galiza, Spain

⁷Laboratori d'Estudis Geofísics Eduard Fontserè, Institut d'Estudis Catalans (LEGEF-IEC), C/ Carme 47, E-08001 Barcelona, Catalonia, Spain

⁸RISKMAT, Institut Geomodels, Universitat de Barcelona, Faculty of Earth Sciences, Department of Earth and Ocean Dynamics, Barcelona, Catalonia, Spain

⁹Laboratorio de Magnetismo de Materiales y Magnetismo Ambiental, Instituto Geográfico Nacional, Real Observatorio de Madrid, C/ Alfonso XII 3, E-28014 Madrid, Spain

¹⁰Departament de Química, Universitat Autònoma de Barcelona (UAB), E-08193 Bellaterra, Catalonia, Spain

¹¹Institut de Ciències de l'Espai (CSIC), Campus UAB Bellaterra, Carrer de Can Magrans s/n, E-08193 Cerdanyola del Vallés, Barcelona, Catalonia, Spain

¹²Institut d'Estudis Espacials de Catalunya (IEEC), Gran Capità 2-4, E-08034 Barcelona, Catalonia, Spain

¹³Geosciences Barcelona (GEO3BCN-CSIC), C/ Lluís Solé i Sabarís s/n, E-08028 Barcelona, Catalonia, Spain

¹⁴Departament de Mineralogia, Museu de Ciències Naturals de Barcelona, Passeig Picasso s/n, E-08003 Barcelona, Spain

¹⁵Institute of Energy Technologies, Department of Chemical Engineering and Barcelona Research Center in Multiscale Science and Engineering, Universitat Politècnica de Catalunya, EEBE, Eduard Maristany 10-14, E-08019 Barcelona, Spain

Accepted 2022 September 29. Received 2022 September 27; in original form 2022 July 30

ABSTRACT

The Traspenna meteorite fell on 2021 January 18 about 20 km south-east of the city of Lugo (Galiza, Spain), shortly after a huge and bright fireball crossed the sky for 4.84 s. Astrometric measurements obtained from the fireball cameras of the Universidade de Santiago de Compostela (USC) as well as from many casual videos were used to determine the atmospheric trajectory of this meteoroid which penetrated the atmosphere and generated sound waves that were detected at three seismic stations. The original meteoroid had a diameter of about 1.15 m and a mass around 2620 kg. It impacted the Earth's atmosphere with a steep entry angle of about 76° from a height of 75.10 km until fading away at 15.75 km with a velocity of 2.38 km s⁻¹. Before the impact, this small asteroid was orbiting the Sun with a semimajor axis of 1.125 au, a moderate eccentricity of 0.386, and a low inclination of 4°55'. A weak evidence of dynamic link with the PHA (Potential Hazardous Asteroid) Minos was investigated. During the atmospheric entry, two major fragmentation events occurred between heights of 35 and 29 km at aerodynamic pressures between 1 and 5 MPa. The strewn field was computed after calculating the individual dark flights of the main body along with two smaller fragments. Fortunately, 2 month after the superbolide, a 527-g meteorite was found. It was examined using several geochemical and petrographic analyses which allowed us to classify it as a moderately shocked (S3) L5 ordinary chondrite with a bulk density of 3.25 g cm⁻³.

Key words: methods: analytical – methods: data analysis – astrometry – Earth – meteorites, meteors, meteoroids – planets and satellites: atmospheres.

1 INTRODUCTION

The fall of meteorites offers a natural way to obtain direct information about the formation and evolution of the minor bodies of the Solar system. Therefore, in addition to the petrochemical analysis, the

knowledge provided by the study of the body entering the atmosphere and suffering ablation before landing, as well as that derived from its heliocentric orbit, are essential to attain a full understanding of the meteoroids at the origin of these phenomena. Furthermore, this type of studies could help us to assess future impact hazards posed by relatively large meteoroids or small asteroids.

Currently, there are a few tens of meteorites with well-computed trajectories and heliocentric orbits. In fact, to our knowledge, 43

* E-mail: manuel.andrade@usc.gal

instrumentally documented fireballs related to recovered meteorites with calculated pre-entry heliocentric orbits have been published up to now. Only one of them was recovered in Spain, the ordinary chondrite Villalbedo de la Peña (Llorca et al. 2005; Trigo-Rodríguez et al. 2006; Llorca, Gich & Molins 2007). There was a second fall, that of the Puerto Lápice eucrite (Llorca et al. 2009; Trigo-Rodríguez et al. 2009), for which no measurements of the meteoroid velocity through the atmosphere were available and it was therefore not possible to calculate its heliocentric orbit. Hence, every instrumentally documented fireball that ends with the fall of a meteorite deserves to be carefully analysed.

In this paper, we investigate the superbolide (with an estimated absolute magnitude of -17 ± 2) observed at 00:18:56.54 UTC on Monday 2021 January 18 that produced the meteorite that fell at about 20 km south-east of the city of Lugo (Galiza, Spain). This would be the first documented fall of a meteorite in Galiza for which it has been possible, in addition, to calculate the atmospheric trajectory, the strewn field, and the heliocentric orbit previous to the impact. This huge and bright fireball was successfully recorded by the cameras of the two stations of the *Universidade de Santiago de Compostela* (USC) dedicated to the observation of fireballs and meteors which are located in Lugo and Santiago de Compostela. In addition, several casual video records of the superbolide were obtained by many private security cameras, one of which also made a sound recording of the sonic booms. Moreover, three seismic stations in the region detected direct sonic waves.

In the course of this research, new mathematical models and an original software have been developed at the *Escola Politécnica Superior de Enxeñaría* (EPSE–USC) to accurately calculate the heliocentric orbit, the fireball atmospheric trajectory, the dark flight, and the strewn field using well-known methods and some novel approaches which are described in detail. This software computes orbital and dynamical parameters, together with their uncertainties, using optimization techniques and Monte Carlo simulations. In fact, the latter have been intensively used in this research as a standard method to routinely obtain the uncertainties of all parameters.

As a result, the expected meteorite strewn field has been derived and the calculated impact point of the main body compared with the actual position of the only recovered meteorite. This was found by chance by an inhabitant of the region 2 month after the fall and it has been classified as an L5 ordinary chondrite.

The paper is organized as follows. Section 2 contains a description of the observational data and astrometric methods. In Section 3, we provide a complete analysis of the superbolide trajectory and its photometric and dynamical characterization, including as well an acoustic and seismic analysis of the sonic booms and the shock wave coupled to the ground. The meteorite fall, including the dark flight, the computation of the strewn field, and the meteorite recovery, is described in Section 4. In Section 5, the heliocentric orbit of the parent asteroid of the Traspenna meteorite is presented together with a discussion concerning potential dynamic associations with near-Earth objects (NEOs). Petrography and geochemical composition of the meteorite as well as their mineral chemistry and classification are given in Section 6. Finally, main results and conclusions are outlined in Section 7.

2 OBSERVATIONAL DATA

The outstanding fireball associated to the Traspenna meteorite fall, named after a small village (meaning *behind the rock* in Galizan Portuguese) located in the Neira river valley (Galiza, Spain) where

the meteorite was found, occurred at 00:18:56.54 UTC (01:18:56.54 local time) on Monday 2021 January 18 and lasted for 4.84 s.

Due to the bad weather conditions (see Fig. 1), only reliable astrometric measurements of the bolide were obtained at the beginning and at the end but scarcely mid-way. However, it was possible to obtain an uncalibrated light intensity curve for most of the bolide, including the main flares. Preliminary results of the computed pre-atmospheric velocity and the slope of the trajectory indicated a high probability of a meteorite-dropping fireball. The same day of the fall, we estimated a nominal impact point close to the village of Lebruxo, in the municipality of Baralla (Lugo). Luckily for us, this location is only about 20 km from the campus of Lugo (USC).

2.1 Eyewitness observations

As far as we know, and mainly due to the restrictions imposed by the emergency pandemic situation on account of COVID-19, there was only one direct eyewitness, a resident of the city of Lugo who was fortunate to see the fireball from the terrace of his penthouse. He described the phenomenon as a bluish-white ball that came out of the sky and briefly made it appear to be daytime.

Moreover, many other people inside their homes also reported huge and powerful flashes and countless people in an area of at least 15 000 km² heard the sonic booms and even woke up frightened in the middle of the night. Many of them reported that they thought it was a thunderclap or even an earthquake that was shaking the windows of their houses.

2.2 Video recordings

2.2.1 Dedicated CCD cameras

The superbolide was recorded by four dedicated CCD cameras in the stations of Lugo, Santiago de Compostela, Madrid, and Estepa (Seville), all of them mounting wide-field video cameras (Madiedo et al. 2009). However, only the first two (see Table 1) that belong to the USC allowed us to obtain sufficiently accurate measurements to be taken into account in the calculations after applying the appropriate astrometric reduction procedure. We note that these two cameras were installed after the daytime superbolide observed over Galiza some years ago for which, unfortunately, it was not possible to determine a reliable atmospheric trajectory which could have allowed finding the meteorites that supposedly could have fallen in the North Region of Portugal (Docobo et al. 2008).

Although that night it was foggy in Lugo, the south-facing camera (the nearest camera to the bolide, only about 20 km from the end of that) was able to record the bolide from almost its beginning until just before its end. Since most of the meteor flares are perfectly visible on this camera, it was used to synchronize all casual videos (with ratios from 15 to 60 frames per second) with an accuracy well below one-tenth of a second as well as to obtain an uncalibrated light intensity curve of the bolide. Unfortunately, weather conditions were not much better at the second nearest station in Santiago de Compostela, as the sky was almost overcast that night as well. Nevertheless, the initial part of the bolide (about 0.64 s) could be perfectly recorded on video thanks to a gap in the clouds and it was useful to measure the meteoroid velocity at the beginning of the atmospheric trajectory and to calculate its pre-atmospheric velocity. The astrometric reductions of all observations recorded at the USC stations were performed at the *Escola Politécnica Superior de Enxeñaría* (USC).

The recordings from the stations located in Madrid and Estepa (Seville) are visually impressive, mostly the latter, considering that

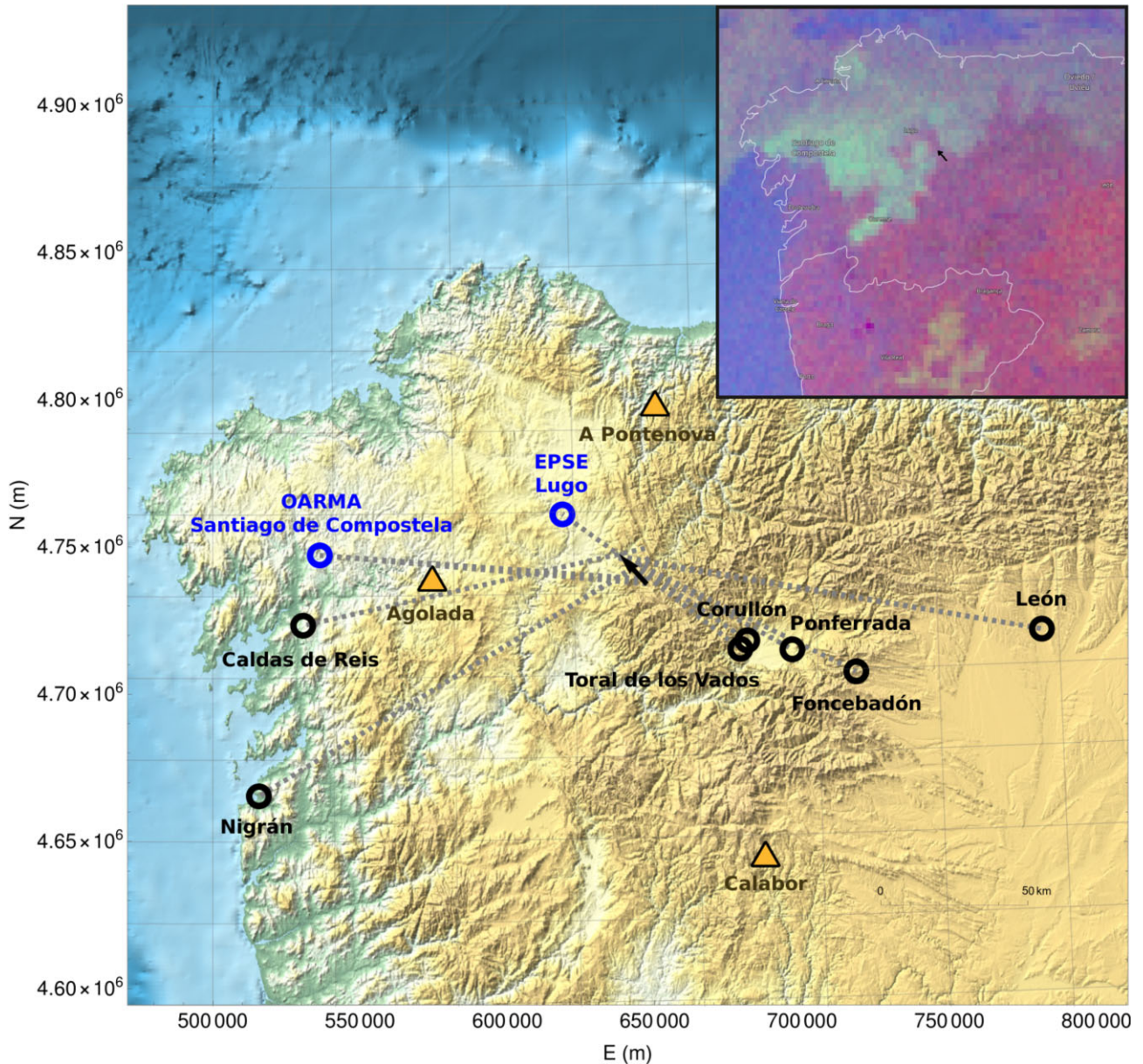


Figure 1. Location map of the Traspesa superbolide. Annuli show the positions of the two USC fireball stations (in blue) and those of the casual cameras (in black) where the superbolide was recorded. Dashed grey lines indicate the lines of sight used in calculations. On the other hand, triangle symbols indicate the positions of the seismic stations where a seismic signal was detected. The ground projection of the atmospheric trajectory is represented by a black arrow in the middle of a map of the NW of the Iberian Peninsula (CRS: ETRS89–TM29). Inset shows the weather situation over Galiza (NW of Spain) on 2021 January 18 at 00:15 UTC. Fog and low clouds are shown in green in this RGB composite image (Source: Eumetsat. Projection: spherical Mercator).

Table 1. Geodetic coordinates referenced to the GRS80 (\approx WGS84) ellipsoid and orthometric heights of the USC fireball stations (dedicated to detect bolides and meteors) and the IGN seismic stations.

Station	Latitude ($^{\circ}$)	Longitude ($^{\circ}$)	Height (m)
EPSE	42.99308	-7.54469	419
OARMA	42.87594	-8.55547	240
EAGO	42.80250	-8.08917	497
ECAL	41.94111	-6.73694	948
EPON	43.32694	-7.14917	541

Notes. EAGO: Agolada (Pontevedra); ECAL: Calabor (Zamora); EPON: A Pontenova (Lugo)

they are 400- and 650-km away, respectively. However, they do not allow for sufficiently accurate measurements and thus they were not considered at all in calculations.

2.2.2 Casual video recordings

In addition to the data provided by our stations, some local digital media published several casual recordings of the superbolide on the internet. Many of these were recorded by security cameras which are usually directed downwards, so the recordings mainly correspond to the final part of the superbolide. We selected seven of them: Caldas de Reis and Nigrán in the province of Pontevedra; Corullón, Foncebadón, León, Ponferrada, and Toral de los Vados/Toural dos Vaos in the province of León. All of them have been particularly

useful for tracking the last part of the bolide. Their positions are shown in Fig. 1, where the ETRS89 Transverse Mercator Coordinate Reference System (ETRS-TM29) has been used as recommended for conformal pan-European mapping at scales larger than 1:500 000.

Four of the wide-field video recordings did not have enough reference stars to obtain precise astrometry of the bolide. To solve this, they were calibrated by means of *in situ* measurements with the theodolite of distant landmarks, correcting for the difference in positions when the instrument could not be placed in the exact same spot as the camera. When possible, they were combined as well with astrometric calibrations implementing corrections of geometric lens deformation.

In the case of Nigrán, a novel calibration procedure was also implemented by means of a laser that was used to target the less bright stars in the field and thus consider a larger number of reference stars. The best recording is that of Corullón from where the last part of the bolide was clearly seen at altitudes between 20° and 15° above the horizon. To calibrate this record, given the scarcity of calibration stars in the video, we used several different positions of Vega as a result of its diurnal motion throughout the year. The calibrations of all observations recorded in the casual videos were performed at the *Observatorio Astronómico R. M. Aller* (OARMA–USC).

Nevertheless, the calibration of some video recordings involves additional uncertainties due to an insufficient number of good reference points on the ground and/or calibration stars in the field of view.

2.3 Acoustic and seismic data

An object at high-hypersonic velocity produces sonic booms due to the propagation of a shock wave produced by the meteoroid in the lower atmosphere. In fact, many witnesses close to the trajectory heard sonic booms shortly after the superbolide. Furthermore, strong detonations were recorded 3 min 21.5 s after the end of the superbolide by the microphone of a security camera located in Cueto, a small village close to Ponferrada and located at a geometric distance of 65 km of the mean point in the trajectory where the main flares were observed. Moreover, electrophonic sounds were reported by an eyewitness at the vertical of the municipality of Triacastela where the meteoroid entered the atmosphere. These can be caused by extra low and very low frequency radio emissions generated by plasma turbulence in the fireball wake being transduced into acoustic waves (Keay 1992).

In addition, four seismic stations of the *Instituto Geográfico Nacional* (IGN) recorded tremors compatible in time with the impact of the meteoroid in the Earth’s atmosphere, namely A Pontenova (EPON) in Lugo, Agolada (EAGO) in Pontevedra, Calabor (ECAL) in Zamora, and Lobios (ELOB) in Ourense, although only the first three were found to actually correspond to the shock waves of the meteoroid. Table 1 shows a list of the USC fireball stations and IGN seismic stations involved in this work.

3 THE ATMOSPHERIC TRAJECTORY

3.1 The 3D geometric model of the superbolide

The trajectories of bolides have traditionally been calculated using most commonly either the intersection of planes method (Cepelcha 1987) or the straight least squares (SLS hereafter) method (Borovička 1990). Borovička himself highlighted the loss of information about the uncertainty of individual observations when a plane is calculated for each station as the main disadvantage

of the former. Moreover, he also pointed out its impossibility to compensate for the Earth’s rotation.

In this work, we have developed an approach that takes advantage of Borovička’s idea of considering the minimal distance to all observed lines of sight to find the trajectory. Therefore, every instantaneous measurement of the meteor position is used to obtain its line of sight in that moment which goes from the observer’s tridimensional position to the bolide. Since we are considering an Earth-centred inertial (ECI) reference frame, the method allows us to take into account the time change during the flight of the bolide and thus compensate every measurement of the Earth’s rotation, thereby removing the Coriolis force. In addition, this also avoids the need to correct for diurnal aberration, another effect due to the Earth’s rotation caused by the change in the observer’s perspective.

Thus, we compute the atmospheric trajectory as the 3D straight line which yields the minimal distance to all lines of sight. In the first instance, to detect potential outliers we consider the ℓ^1 -norm minimization problem (also called least-absolute minimization) rather than the least-squares minimization (i.e. the well-known ℓ^2 -norm or Euclidean norm). The former is more robust and, therefore, less sensitive to outliers. Moreover, it gives equal weight to all observations, unlike ℓ^2 -norm which gives more emphasis to large residuals. In fact, least squares techniques are useful when the observations are subject to random and normally distributed errors. However, if these assumptions are violated, e.g. in cases where observations are affected by systematic errors or outliers, robust estimation techniques produce better results (Rice & White 1964; Kiountouzis 1973). In a second step, when the measurement set is free of outliers, the minimization problem is solved by considering the ℓ^2 -norm.

Consequently, the computation of the minimum distance straight line, $\mathcal{T} \subset \mathbb{R}^3$, has been addressed as a mathematical two-step optimization problem in which we want to minimize distances from every line of sight i to the 3D straight line of the trajectory

$$D_i = D_i(\mathbf{p}_i, \mathbf{s}_i, \mathbf{u}, \mathbf{r}), \tag{1}$$

where $\mathbf{p}_i = (x_i, y_i, z_i) \in \mathbb{R}^3$ is the position of each station in geocentric Cartesian coordinates and $\mathbf{s}_i = (\xi_i, \eta_i, \zeta_i) \in \mathbb{R}^3$ is a unit vector from each station in the direction of each line of sight for $i = 1, 2, \dots, n$ (with n the total number of observations); $\mathbf{u} = (x_u, y_u, z_u) \in \mathbb{R}^3$ is an arbitrarily chosen point on the trajectory; and $\mathbf{r} = (\xi_r, \eta_r, \zeta_r) \in \mathbb{R}^3$ is a unit vector in the direction to the radiant. However, considering that vectors exclusively related to each station are known, the only unknowns will be \mathbf{u} and \mathbf{r} . Hence, we define the objective function

$$\begin{aligned} \|d\|_\eta : \mathbb{R}^3 \times \mathbb{R}^3 &\longrightarrow \mathbb{R} \\ (\mathbf{u}, \mathbf{r}) &\longmapsto \|d(\mathbf{u}, \mathbf{r})\|_\eta = \sum_{i=1}^n w_i \|d_i(\mathbf{u}, \mathbf{r})\|_\eta, \end{aligned} \tag{2}$$

assigning an objective value to each solution, with $\eta = 1$ in the first step (ℓ^1 -norm) and $\eta = 2$ in the second one (ℓ^2 -norm), being w_i the weight of each observation.

Thus, we have to find the solution of the two unconstrained ℓ^n -norm problems

$$\underset{(\mathbf{u}, \mathbf{r}) \in \mathbb{R}^3 \times \mathbb{R}^3}{\text{minimize}} \|d(\mathbf{u}, \mathbf{r})\|_\eta, \tag{3}$$

firstly with $\eta = 1$ and then with $\eta = 2$.

Finally, the solution will be the straight line \mathcal{T} corresponding to the lowest value of the objective function. Instead of using linearization and the gradient method, as in the case of solving the non-linear equations of the SLS method (Borovička 1990), we have solved our minimization problems carrying out parallel processing as a way to speed a large array of global (Nelder–Mead simplex, differential

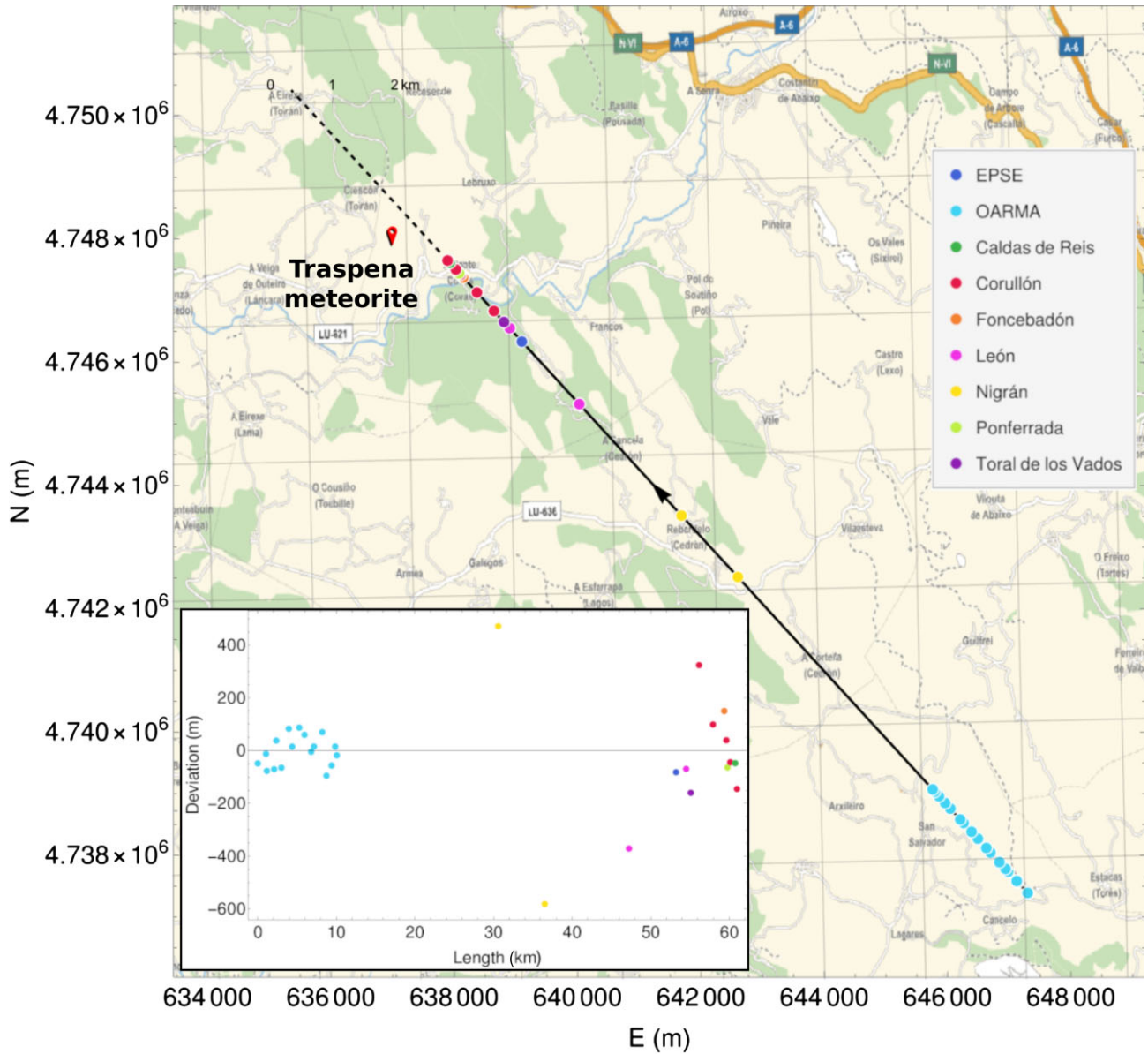


Figure 2. The ground projection of the Traspenna atmospheric trajectory is shown in a map of the region (CRS: ETRS89–TM29) using a solid black line whereas the dashed line indicates the dark flight (without atmosphere). The discs show the positions on the trajectory where the superbolide was observed and their colour indicates the location from which it was observed. The black drop icon marks the actual meteorite fall site whereas the red one indicates the calculated site (we note that they differ by only 31 m so that in the figure they are practically superimposed). Inset on the left bottom shows deviation of each line of sight for each station from the average straight trajectory in an ECI reference frame. The sign is positive if the line of sight crosses vertical plane above the trajectory. Note the different scales on the x and y axes.

evolution, and simulated annealing) and local methods (gradient, conjugate gradient, Newton, BFGS, and principal axis) running in parallel with different sets of parameters. After many simulations, we have seen that methods using derivatives generally fail to reach the minimum value of the objective function if the initial point is not close enough to the solution. Therefore, we have solved the two problems described by equation (3) using primarily global methods which do not require the calculation of derivatives and which have provided us with an excellent initial approximation to the solution. Subsequently, the solution has been refined using local methods as well. In most cases, the method of principal axis of Brent (1973), a derivative-free algorithm with quadratic convergence, has proven to be the best choice together with the differential evolution algorithm (Storn & Price 1997).

We assume that the observations (as well as the ECI Cartesian coordinates) are given in the epoch of date. Geodetic coordinates are referred to the GRS80 ellipsoid (\approx WGS84) and orthometric heights (heights above mean sea level) are calculated using the geoid-ellipsoid separation from the EGM2008 geoid model which yields a value of $+57.0$ m over the entire region. Our calculations are based on 31 lines of sight from 9 different stations covering the full flight since the beginning of the bolide to the end. Measurements of the position of the bolide along its track in the recorded videos were carried out using accurate timing for each frame after a joint synchronization of all recordings.

Deviations of individual lines of sight from the 3D straight trajectory fitted in an ECI reference frame are shown in Fig. 2. The low density of data in the middle part of the trajectory is due to

Table 2. The atmospheric trajectory of the Traspesa superbolide. Geodetic coordinates and azimuth as well as projected length are referenced to the GRS80 (\approx WGS84) ellipsoid. The apparent radiant is given at the beginning of the trajectory.

		Beginning	End
Time (UTC)	t	00:18:56.54 \pm 0.04	00:19:01.38 \pm 0.04
Geodetic latitude ($^\circ$)	φ	42.77488 \pm 0.00047	42.86900 \pm 0.00053
Geodetic longitude ($^\circ$)	λ	-7.1994 \pm 0.0055	-7.3119 \pm 0.0011
Ellipsoidal height (km)	h	75.15 \pm 0.31	15.81 \pm 0.04
Orthometric height (km)	H	75.10 \pm 0.31	15.75 \pm 0.04
Velocity (km s $^{-1}$)	v	15.07 \pm 0.11	2.38 \pm 0.32
Acceleration (km s $^{-2}$)	a	-	-7.28 \pm 0.71
Duration (s)	Δt		4.84 \pm 0.06
Length (km)	Δl		60.98 \pm 0.38
Projected length (km)	Δl_p		14.02 \pm 0.40
Geodetic azimuth ($^\circ$)	A		318.7 \pm 1.4
Slope ($^\circ$)	γ		76.7051 \pm 0.0018
Pre-atmospheric velocity (km s $^{-1}$)	v_∞		16.42 \pm 0.29
Apparent radiant (RA) ($^\circ$)	α_R^{app}		125.49 \pm 0.51
Apparent radiant (Dec) ($^\circ$)	δ_R^{app}		32.334 \pm 0.088
Radiant (constellation)			Cancer

a combination of three factors, namely, the bad weather conditions around some stations, the huge flares observed in that part of the trajectory which saturated the frames even for the most distant cameras and, as we already said, to the fact that the casual recordings obtained by the security cameras are mainly directed towards the ground. Anyhow, the relatively low dispersion of the data would indicate that there are no large errors in the calibration of the videos.

The asteroid hit the atmosphere from the southeast and began to be observed at a height of 75.10 km, with an average slope of $76^\circ 7051$ to the horizon, at a velocity of 15.07 km s^{-1} . After 4.84 s, and a flight of 60.98 km, the fireball disappeared at a height of 15.75 km with a velocity of 2.38 km s^{-1} .

We have developed a Monte Carlo approach for propagating trajectory uncertainties from the observed astrometric positions (altitudes and azimuths) of the bolide. As usual, we have considered 10^4 random samples of these positions assuming a Gaussian distribution for each coordinate with a standard deviation equal to three times the uncertainty of each of them. Then, we have calculated an optimal atmospheric trajectory for each sample using the above-mentioned method. Accurate values of the parameters characterizing the atmospheric trajectory along with their uncertainties are shown in Table 2.

The median absolute deviation of the fit is only 70 m. On the other hand, considering that the trajectory is really slanted and that the duration of the bolide is quite short, the expected bending due to the Earth’s gravity is indeed very small, roughly 100 m at most.

The atmospheric trajectory projected on the ground is plotted in Fig. 2. It runs entirely through the foothills of the Os Ancares mountain range. The beginning is located at the vertical of the municipality of Triacastela. The fireball continued to fly over the municipality of Lánara to finish in that of Baralla.

3.2 Velocity fit

The length travelled from the beginning of the bolide as a function of time was obtained from the projection of each measurement on the calculated trajectory. This was counted from the first measurement on the video recorded at the OARMA station to the last measurement obtained at Corullón. Lengths corresponding to the first 2.88 s, before main fragmentation events (see Section 3.7), have been calculated ac-

ording to Whipple & Jacchia (1957) by fitting the exponential model

$$L_1 = a_1 + b_1 t + c_1 e^{k_1 t}, \tag{4}$$

where L_1 is the length of the fly, t is the time since the beginning, and $a_1, b_1, c_1,$ and k_1 are coefficients to be calculated.

Nevertheless, considering that this bright bolide has survived until reaching a significant low height, even after having undergone a severe fragmentation and a strong deceleration, we have supposed that in the last part of its trajectory (11 observations during 1.51 s before the end) the meteoroid was being uniformly decelerated and thus we have fitted the quadratic model (McCrosky et al. 1971)

$$L_2 = a_2 + b_2 t + c_2 t^2, \tag{5}$$

where L_2 is the length of the last part of the fly, t is the time since the beginning of this part, and $a_2, b_2,$ and c_2 are coefficients to be calculated.

Continuity has been imposed as a condition on the length travelled by the meteoroid and on its first derivative with respect to time. However, we found that although imposing second-derivative continuity results in the velocity becoming a smooth function of time, the model does not fit well the dynamic behaviour of the bolide in the final part. In fact, we suppose that the acceleration may have changed abruptly in this final part as a result of the fragmentations suffered by the main body of the meteoroid until reaching a constant value.

From the fittings given by equations (4) and (5), we can straightforwardly obtain velocities and accelerations. Length depending on time is shown in Fig. 3. We observe that the bolide was clearly decelerated at lower heights until reached a final velocity of 2.38 km s^{-1} .

On the other hand, the very first observation of the bolide corresponds to that recorded at the OARMA station between the clouds covering most of the field of view at that moment. Therefore, the pre-atmospheric velocity v_∞ in the geocentric inertial reference frame was obtained using a linear fit of the measurements derived from the first 17 frames of the video recorded at the OARMA station during the first 0.64 s. We assume that this was the velocity at which the meteoroid impacted the Earth’s atmosphere. This impact would have taken place at a height of about 120 km, as we can make the assumption that atmospheric effects are negligible above this height (Egal et al. 2017).

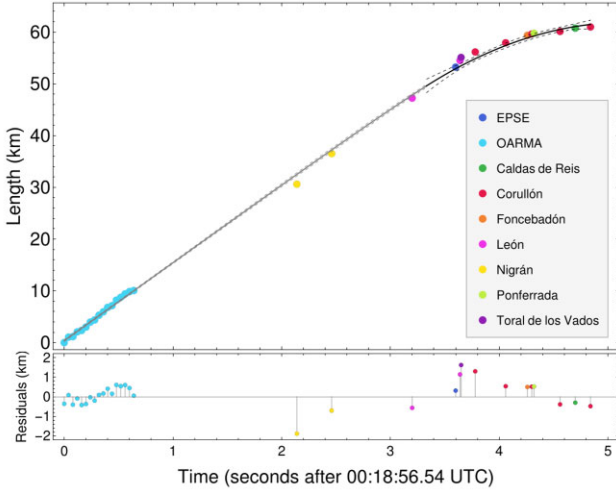


Figure 3. Length modelled according to L_1 (in grey) and L_2 (in black) along the trajectory as a function of time. Confidence bands at 1σ are plotted as well. Residuals for each measurement are shown in the bottom part of the plot.

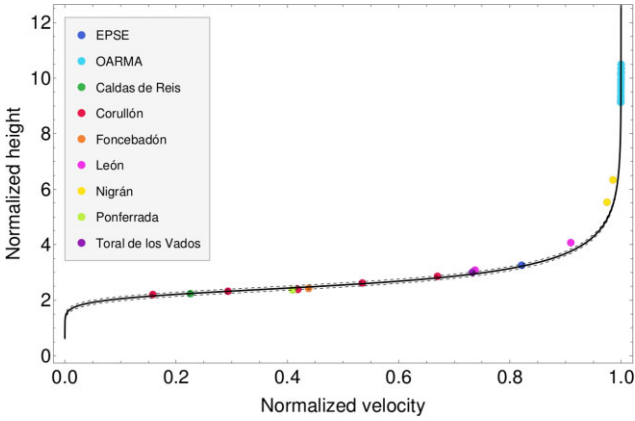


Figure 4. Plot of observational data with velocity normalized to initial velocity ($v_0 = 15.07 \text{ km s}^{-1}$, in this case) and height normalized to the atmospheric scale height (usually, $h_0 = 7.16 \text{ km}$). The solid black line shows the analytic solution $y(v)$ of the meteor physics equations given in Gritsevich (2007). Uncertainty bands derived from the 5-per cent trimmed variance for this fit are plotted as well.

Velocities at the beginning and at the end of the bolide, as well as the pre-atmospheric velocity, are shown in Table 2.

3.3 Dynamics of the atmospheric flight: the dimensionless coefficient method

The atmospheric flight has been parametrized using the dimensionless coefficient method devised by Gritsevich (2007) from the equations describing the trajectory that Stulov (1997) introduced. Therefore, considering the heights and the velocities derived from the geometric trajectory, the dynamics of the bolide can be characterized by two parameters, namely the dimensionless ballistic α and the mass-loss β parameters. Moreover, since no reliable photometric information is available in this case, the application of this method derived from the meteoroid dynamic equations is the only way to accurately calculate the meteoroid mass along the entire trajectory. On the other hand, we assume that the fact that the meteoroid has undergone several fragmentations in the last part of the bolide has no noticeable implications for the description of the motion, since the

application of a single body theory would still be valid to describe the motion of the largest surviving body.

This method uses the theoretical height–velocity relation derived from the equations of the meteoroid motion in order to define a function that contains all the dynamic information about the motion through the atmosphere

$$F_i(y_i, w_i, \alpha, \beta) = 2\alpha e^{-y_i} - \Delta_i e^{-\beta},$$

$$\text{with } \Delta_i = \overline{Ei}(\beta) - \overline{Ei}(\beta w_i^2), \quad i = 1, 2, \dots, n, \quad (6)$$

where

$$\overline{Ei}(x) = \int_{-\infty}^x \frac{e^z}{z} dz,$$

is the exponential integral function. On the other hand, $y_i = h_i/h_0$ (with $h_0 = 7.16 \text{ km}$, as usual, being the scale height of the homogeneous atmosphere) and $w_i = v_i/v_0$ (with v_0 being the initial velocity at the beginning of the luminous trajectory) are the normalized heights and the normalized velocities, respectively, and n is the total number of observations.

Estimates for α and β are customary obtained by applying the least-squares method to the equation (6). The usual resolution algorithm (Gritsevich 2009) consists in first numerically estimating β from the extremum condition and then calculating α from that. This iterative procedure is continued until the solutions are close enough to the desired minimum.

Nevertheless, we have solved the problem by searching directly for the global minimum using the same minimization techniques described above for obtaining the equation of the 3D atmospheric trajectory (see Section 3.1), thereby α and β have been calculated simultaneously checking that the values obtained really correspond to the global minimum.

Considering that heights and velocities for each observation are known, the only unknowns will be α and β . Hence, we define the objective function

$$Q: \mathbb{R}^2 \rightarrow \mathbb{R}$$

$$(\alpha, \beta) \mapsto Q(\alpha, \beta) = \sum_{i=1}^n [F_i(y_i, w_i, \alpha, \beta)]^2. \quad (7)$$

Thus, we have to find the solution of the constrained problem given by

$$\begin{aligned} &\text{minimize } Q(\alpha, \beta) \\ &(\alpha, \beta) \in \mathbb{R}^2 \end{aligned} \quad (8)$$

subject to $\alpha > 0$, $\beta > 0$.

Some measurements were discarded, not because they did not fit a hypothetical trajectory from a geometrical point of view, but because they did not verify the constraints imposed by the meteoroid dynamic equations, probably due to errors in heights or to time inconsistencies in the recordings. This means there is no solution for α and β compatible with such a set of measures. Usually, α and β parameters are calculated without providing any estimate of their uncertainties. In order to assess these, we have carried out a novel statistical analysis using the 5-per cent trimmed variance, a robust measure of dispersion. The α – β diagram is shown in Fig. 4 and results are listed in Table 3.

From these parameters, we can obtain the initial mass of the meteoroid which depends on α

$$M_0 = \left(\frac{1}{2} \frac{c_d A_0 \rho_0 h_0}{\alpha \rho_m^{2/3} \sin \gamma} \right)^3, \quad (9)$$

where γ is the slope of the meteoroid flight to the horizontal, h_0 is the scale height of the homogeneous atmosphere, ρ_0 the atmospheric

Table 3. Parameters of the Traspenna atmospheric flight: assumed atmospheric surface density, drag coefficient, initial shape coefficient, shape change coefficient, and actual measured value of the meteoroid bulk density are indicated in the first five rows. In addition, initial kinetic energy, maximum aerodynamic pressure (and time of that), ablation coefficient, ballistic and mass-loss parameters, as well as mass and size are also summarized in the next rows.

Parameter	Source	
ρ_0 (kg m ⁻³)	1.2250	ISA ^a
c_d	1.84	Ideal sphere
A_0	1.209	Ideal sphere
μ	2/3	Uniform mass-loss
ρ_m (g cm ⁻³)	3.25 ± 0.01	Actual measured value
Initial kinetic energy, maximum aerodynamic pressure, and ablation		
E_k (J)	(3.53 ± 0.86) × 10 ¹¹	(= 0.0844 ± 0.0206 kt TNT)
P_{\max} (MPa)	7.84 ± 0.23	
t (P_{\max}) (s)	3.65	
σ (s ² km ⁻²)	0.0652 ± 0.0053	
Ballistic and mass-loss parameters		
α	3.32 ± 0.26	
β	2.47 ± 0.20	
Mass and size		
	Beginning	End
M (kg)	(2.62 ± 0.63) × 10 ³	1.9 ± 1.2
\varnothing (m)	1.15 ± 0.09	0.10 ± 0.02

Note. ^aAcronym of *International Standard Atmosphere* (ISO 2533:1975)

surface density, c_d is the drag coefficient, A_0 the initial shape coefficient ($=S_0/W^{2/3}$, being S_0 the initial cross-sectional area and W the body volume), and ρ_m the meteoroid bulk density.

The instant mass of the meteoroid is obtained, as usual, after integrating the fundamental equations of meteoroid motion and ablation (Bronshten 1983). That is

$$M(t) = M_0 e^{\frac{\sigma}{2} [v(t)^2 - v_0^2]}, \quad (10)$$

where v_0 is the initial velocity at the beginning of the luminous trajectory, $v(t)$ the instantaneous velocity in time t , and σ the ablation coefficient. Moreover, this instant mass is related to β since

$$\sigma = \frac{2\beta}{(1 - \mu)v_0^2}, \quad (11)$$

where μ is the shape change coefficient representing the rotation of the meteoroid ($0 < \mu < 2/3$).

The ablation coefficient is nearly constant for homogeneously composed bodies that undergo progressive ablation during the atmospheric trajectory. Regarding the meaning of μ , if $\mu = 0$, thus, there is no spin while $\mu = 2/3$ indicates that fast rotation may allow equal ablation over the entire meteoroid surface so that no change in the shape of the object is expected, i.e. it would be self-similar. The latter is the usual assumption based on experience (Bouquet et al. 2014) as it represents a uniform mass-loss of the body over the entire surface area. The expression given in equation (10) provides the final mass at the terminal height of the bolide. Thus, neglecting ablation after this point, this would be, if it exists, also the final mass of the meteorites.

The assumed values for all the unknown parameters during the atmospheric trajectory as well as the masses and diameters together with the ablation coefficient derived from them are summarized in Table 3. In addition, maximum dynamic pressure and impact energy are also listed. These parameters can also be used to estimate how

Table 4. Physical features of each detonation in the sonic booms: time since the beginning of the first detonation, duration, average frequency, and relative sound pressure level are listed.

Detonation	t (s)	Δt (s)	f (Hz)	L_p (dB)
1	0.000	0.032	510 (C5)	−30.6
2	0.041	0.026	579 (D5)	−31.7
3	0.119	0.046	584 (D5)	−32.1
4	0.365	0.039	566 (C#5)	−35.4
5	0.589	0.069	350 (F4)	−34.5
6	0.710	0.052	306 (D#4)	−35.6
7	0.794	0.048	333 (E4)	−36.7

likely a fireball is to be a meteorite-dropping candidate (Gritsevich, Stulov & Turchak 2012; Sansom et al. 2019).

Our calculations show that the shape of the trajectory in normalized velocity–height variables (see Fig. 4) can be successfully fitted to the trajectory of a single body with ablation. This would indicate that the fragmentation, although clearly observable in the videos, does not significantly affect the shape of the trajectory in the velocity–height variables. This behaviour has been reported in the past (Stulov 2000) and it could be due, as Barri & Stulov (2003) suggest in the case of the Benešov fall, to the fact that the initial masses of the separated fragments before the ultimate break-up of the body are small compared to the mass of the main body. In fact, according to Barri (2010), a single body model with ablation would be the best approximation of an observation trajectory when the mass lost due to ablation is greater than the total initial mass of fragments. Anyway, we must take into account that in both studies β is derived from the ablation coefficient σ setting the shape change coefficient to $\mu = 0$, that is, considering a non-rotating meteoroid.

3.4 Acoustic analysis

In the audio recording mentioned in Section 2.3, the silence of the night can be heard to be broken by the sonic booms caused by the meteoroid entering the atmosphere immediately followed by the barking of dogs mixed with a long rumbling sound extending over several seconds. This is a bizarre scenario very similar to that described by Öpik (1970) commenting on the first audio recording of the sonic boom caused by a meteoroid penetrating the Earth’s atmosphere and which resulted in the Boveedy meteorite (Northern Ireland) on 1969 April 25. As far as we know, this would be one of the few historical records of the sonic booms of a meteoroid entering the Earth’s atmosphere and resulting in a meteorite.

Sonic booms were recorded 3 min 21.5 s after the end of the bolide by a security video camera equipped with a microphone in Cueto (León), a small village close to Ponferrada and located at a geometric distance of 65 km of the mean point in the trajectory where the main flares of the bolide were observed. The first detonation is the strongest as well as the most complex since it is composed of a powerful start immediately accompanied by two weaker detonations that seem to sound almost at once. Then another detonation is heard followed by three more rapid detonations. Typically, these sonic booms are caused by a cylindrical blast wave originating from the closest point on the trajectory. An acoustic analysis of the signal has been carried out in order to determine its most relevant physical features. Results are summarized in Table 4 whereas the waveform and the spectrogram of the acoustic signal for the first second are shown in Fig. 5.

Furthermore, taking into account the physical features of the acoustic signal, one of us (MA) has written down the approximate

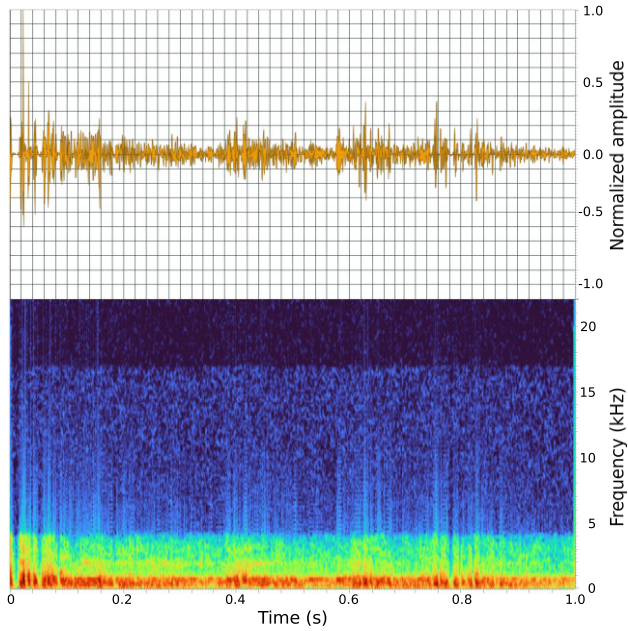


Figure 5. Waveform (top) and spectrogram (bottom) of the first second of the acoustic signal corresponding to the sonic booms caused by the entry of the meteoroid into the Earth’s atmosphere (recorded from Cueto about 3 min 21.5 s after the end of the bolide).

music, changing only the tempo, that this small asteroid produced when it entered the Earth’s atmosphere. That is



3.5 Seismic analysis

The entry of meteoroids in the atmosphere generates infrasound waves by means of two mechanisms: hypersonic flow and fragmentation. Infrasound frontwaves travel through the atmosphere being refracted and guided over long distances in a way highly dependent on the temperature and humidity gradient as well as on the wind profile (Kulichkov 2004; Silber et al. 2009). In addition, the sonic wavefront undergoes the decay of energy with distance in its propagation through the air and subsequent interaction with the ground, becoming seismic waves and making possible its detection by seismic stations in the neighbourhood (Edwards, Eaton & Brown 2008). To detect sonic waves coming from an atmospheric phenomenon, infrasound stations are needed, not necessarily nearby, as the networks of these infrasound stations are very extensive due to the fact that the sonic wave travels a long distance with little attenuation. On the other hand, to detect seismic waves, seismic stations are needed fairly close to the event, as seismic waves suffer more from energy attenuation with distance.

No measurements have been found at the infrasound stations nearest to the Traspenna meteoroid trajectory. On the other hand, there are nine seismic stations in the surroundings owned by the Spanish Digital Seismic Network operated by the *Instituto Geográfico Na-*

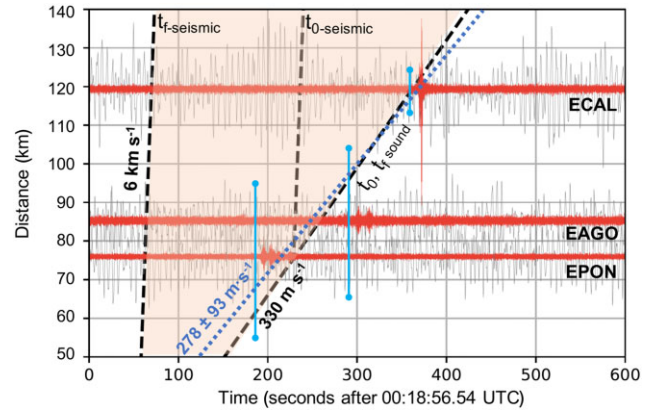


Figure 6. Seismic record section. Raw seismic data (grey waveforms) from IGN seismic stations (EPON, EAGO, and ECAL) are plotted together with processed seismic data (red waveforms) and placed at the mean distance to the atmospheric trajectory. The vertical blue lines represent the width of the source–station distance for the entire trajectory. The dashed black lines indicate the values of the time model. The line labelled as ‘ t_0, t_f sound’ represents a wave travelling at a sound velocity of 330 m s^{-1} directly arriving at each seismic station from the initial and the end time of the trajectory (since for a wave travelling at the speed of sound, the differences between the arrival times from the start and end of the trajectory are small and they are represented as a single line of 330 m s^{-1}). The lines labelled as ‘ t_0 -seismic’ and ‘ t_f -seismic’ represent, for the initial and final time of the trajectory, a wave that starts propagating as a sound wave and upon impacting the ground continues its journey to each seismic station as a seismic wave at 6 km s^{-1} . The light orange region shows the region compatible with seismic detections. The dashed blue line is the weighted regression line which provides the sound speed ($278 \pm 93 \text{ m s}^{-1}$) considering the experimental seismic time arrivals and distance ranges.

cional, Spain (1999). All these stations are equipped with broadband instruments with nearly flat velocity responses between 0.01 and 50.0 Hz and a sampling rate of $100 \text{ counts s}^{-1}$.

The raw data from these nine seismic stations did not show at first glance any notable events compatible with the bolide. In fact, these had to be detrended and 3-Hz high-pass filtered using Obspy/PYTHON (Krischer et al. 2015) to find events compatible with the bolide. Finally, only four stations presented events that could be compatible with the meteoroid flight, which are as well the nearest stations (EPON, EAGO, ECAL, and ELOB). The remaining stations did not record any events due to distance (beyond 130 km) or low signal-to-noise ratio.

The raw and processed seismic data together with a synthetic model of the sonic and seismic wave coming from the meteoroid flight are shown in Fig. 6. First, the threshold of a sonic wave emitted from the beginning to the end of the bolide and propagating homogeneously in the atmosphere with a velocity of 330 m s^{-1} is depicted. Because of the hypersonic velocity of the meteoroid, the emission of sound waves at the starting and final points of the trajectory, propagating both at the speed of sound, are practically indistinguishable ($t_{0\text{-sound}}, t_{f\text{-sound}}$). The thresholds of the combined sonic and seismic wave propagation for the initial ($t_{0\text{-seismic}}$) and final ($t_{f\text{-sound}}$) emission are represented by a high seismic velocity of 6 km s^{-1} as an upper limit. In addition, due to the hypersonic velocity of the meteoroid flight and the fast descent in height, the seismic waves emitted at the end point were detected at the seismic stations earlier than those emitted at the start point. According to this velocity model, EPON, EAGO, and ECAL stations (see Table 1) are

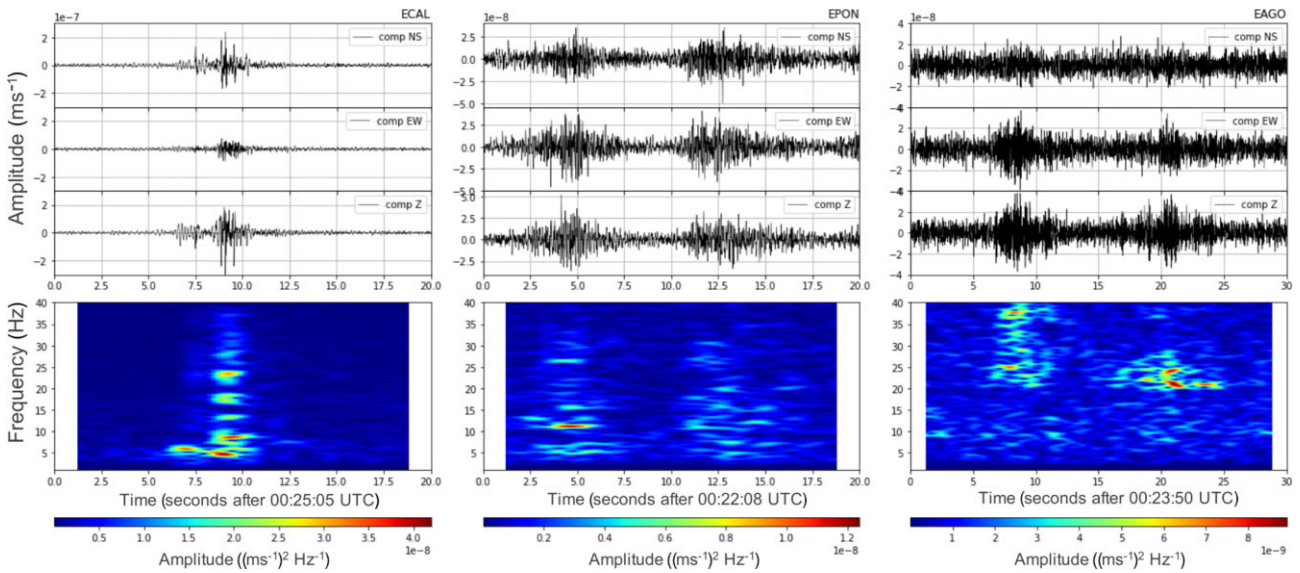


Figure 7. Three-component seismic waveform (NS, EW, and Z vertical component) of each station together with its vertical component spectrogram calculated with a window length of 2 s for the Fast Fourier Transform (FFT) and 95-per cent overlap.

compatible detections with direct sonic wave coupling to the station ground and with the source–station distance range (see Fig. 1).

Thus, ECAL, the farthest station although aligned with the trajectory, clearly agrees with this hypothesis. On the other hand, EAGO and EPON, the closest stations located crosswise to the trajectory, are more sensitive to the variation of the moving source and, at first glance, it is difficult to estimate the type of detection they have made. However, the similarity of the EPON and EAGO events leads us to conclude that in their distance ranges, compatible with the trajectory of the bolide, it is most plausible that they are the same direct wave detection.

A weighted linear regression fitting the arrival times of the events of these three stations, taking into account the variability of the distance to the source for each of them, gives a wave velocity value of $278 \pm 93 \text{ m s}^{-1}$ which is compatible with a sound wave velocity. Therefore, the recorded event in ELOB is discarded because this detection does not correspond to any consistent arrival time with the meteoroid moving source. In fact, a more detailed observation of the characteristics of the ELOB event suggests that it would be a very small local earthquake, detected only at this station and not identified in any seismic catalogue.

The three component time data of EPON, EAGO, and ECAL, together with a spectral analysis using the spectrogram representation, are shown in Fig. 7. We observe that the sharpest signal belongs to the ECAL station, although it is the most distant one, with a detection duration of about 6 s, which is also consistent with the astronomical estimates. ECAL presents a clear directivity phenomenon, showing higher amplitudes in the NS component than in the EW. Precisely, this station is approximately located in the NS direction of the trajectory, which is also predominantly NS. On the other hand, EPON and EAGO are stations almost equidistant from the trajectory, EAGO to the west and EPON to the east, transverse to the direction of the bolide. Both stations present a double event very similar to each other, also with a duration of 6 s, although in this case, we believe that this double event is due to an echo phenomenon. The frequency content of ECAL and EPON is compatible with each other, with the main amount of energy concentrated up to 15 Hz. However, EAGO does not seem to fit well with ECAL. In fact, an analysis of the data

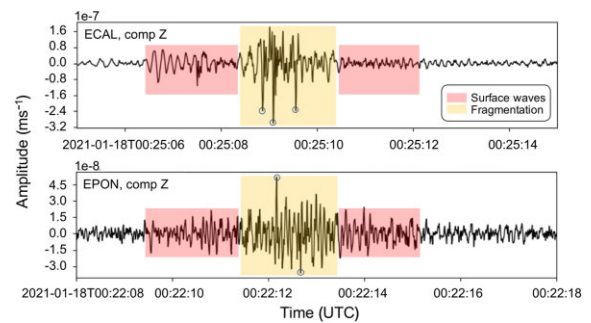


Figure 8. Vertical components of ECAL and EPON. The red boxes indicate the surface-type waves: the first box indicates the precursor Rayleigh waves and the second one indicates the induced Rayleigh waves that become seismic noise level. The yellow boxes identify the part of the signals generated by the main ablations of the Traspenna meteoroid. The N-type signal, corresponding to the fragmentation events, is easily recognizable in the vertical component of the ECAL. The blue circles indicate the amplitudes considered to calculate the magnitudes.

from the former shows that the records at this station systematically lack a significant frequency content up to 20 Hz, which could be due to the particular local conditions.

Observing the time histories of the vertical components of EPON and ECAL (see Fig. 8), we can identify surface waves from the hypersonic entry of the meteoroid and longitudinal waves with predominant amplitudes due to fragmentations with the characteristic N pattern (Edwards et al. 2008; Silber et al. 2018). If we consider an approximation with the scale of magnitudes of earthquakes for the Iberian Peninsula (IGN m_{bLg} scale of magnitudes, referred to Richter’s local magnitude formula), the maximum amplitudes in the seismic record of ECAL correspond to magnitudes of 1.7–1.8. In the case of EPON, its maximum amplitudes correspond to magnitudes of 0.6–0.7. These magnitudes were transformed to energy using the seismic energy law of Gutenberg & Richter (1956) expressed in ergs ($\log E_s = 2.4 m_b + 5.8$) for body wave magnitudes. The resulting energies for each fragmentation are around $E_s = (0.8\text{--}1.3) \times 10^6 \text{ J}$

for ECAL and $(2-3) \times 10^3$ J for EPON. It is difficult to separately identify the different fragmentations in these seismic records and perform a total estimate of the energy. Nevertheless, taking into account that the transmission of a sonic wave that propagates in the air and becomes a seismic wave in the ground is considered very inefficient, we can correct the energy of these main fragmentations using a factor between 0.01 and 0.1 per cent (Brown et al. 2002a). We have considered the lowest transmission which provides energies around $(0.8-1.3) \times 10^{10}$ and $(2-3) \times 10^7$ J, respectively, for each fragmentation.

The ECAL and EPON magnitudes do not correspond to each other, but this may be due to the fact that the seismic magnitudes are fitted to a seismic velocity model of the subsurface and not to a sonic velocity model for the atmosphere. The distance corrections implicit in the magnitude calculations as well as the atmospheric profile may vary appreciably with azimuth in the case of Traspenna. In addition, we have no information on the atmospheric profile as a function of the temperature, pressure, and humidity depending on height and azimuth which prevents us from deriving a reliable model of sonic velocities. This also implies the impossibility to perform a source localization using only the three seismic data detections (Edwards & Hildebrand 2004) and that is why a direct approach to the problem using a synthetic model adapted to the characteristics of the bolide trajectory was chosen. This lack of information could also explain the differences in the time arrivals between EAGO and EPON observed in Fig. 6.

3.6 Mass-loss model and maximum ablation regime

The expression given in equation (10) provides meteoroid mass depending on time by means of its velocity in each time. However, to analyse mass-loss during the atmospheric trajectory, it would be more useful an expression that would give us the mass explicitly as a function of time. We have considered that evolution of time-dependent variables in many physical phenomena can be modelled accurately by the hyperbolic tangent function

$$\pm \tanh x \equiv \frac{e^{\pm x} - e^{\mp x}}{e^{\pm x} + e^{\mp x}}, \quad x \in \mathbb{R}. \quad (12)$$

This is an odd and symmetric function with continuous monotonous increase/decrease that, in addition, as a rational function of the exponential function exhibits interesting asymptotic properties. In this regard, we have experimentally verified that the hyperbolic tangent function under the assumption that the meteoroid mass is a monotonically decreasing function of time is a valid empirical model that fits very well the smooth meteoroid mass variation due to ablation as it passes through the Earth's atmosphere.

On the other hand, it is well-known that the hyperbolic tangent satisfies the following first-order non-linear differential equation

$$w'(x) + w(x)^2 - 1 = 0, \quad \text{with } w(x) = \tanh x, \quad \forall x \in \mathbb{R}. \quad (13)$$

With this in mind and trying to find a physical explanation for the good fit, we hypothesize that the mass-loss of the meteoroid as it passes through the Earth's atmosphere is proportional to the difference between the square of a certain value of the mass A , the interpretation of which will be given later, and the square of the rescaled mass at each instant of time $\mathcal{M}(t)$. Therefore, we propose a mathematical model for the mass-loss of the form of the first-order initial-value problem

$$\mathcal{M}'(t) = \kappa [A^2 - (\mathcal{M}(t) - B)^2], \quad \text{with } \mathcal{M}(0) = \mathcal{M}_0, \quad (14)$$

where \mathcal{M}_0 is the initial mass, $\kappa \in \mathbb{R}^-$ is a constant of proportionality and $A, B \in \mathbb{R}^+$ are parameters to adjust the mass scale.

This differential equation is of the type known as the special Riccati equation and it is integrable by quadrature in terms of elementary functions. Thus, the solution of the problem posed by the equation (14) can be obtained analytically after a few mathematical manipulations and simplifications in the form

$$\mathcal{M}(t) = A \tanh \left[A \left(\kappa t + \frac{C}{B^2} \right) \right] + B, \quad t \in \mathbb{R}, \quad (15)$$

where κ, A, B , and C are constant parameters to be determined, the latter arising as an arbitrary constant resulting from the integration of (14). Regarding their physical interpretations, we see that parameters A and B are given by

$$A = \frac{\mathcal{M}(-\infty) - \mathcal{M}(+\infty)}{2}, \quad (16)$$

$$B = \frac{\mathcal{M}(-\infty) + \mathcal{M}(+\infty)}{2},$$

where $\mathcal{M}(-\infty)$ and $\mathcal{M}(+\infty)$ are the asymptotic values of the masses when $t \rightarrow -\infty$ and $t \rightarrow +\infty$, respectively. We note that in most cases, mainly for large meteoroids with $\mathcal{M}(-\infty) \gg \mathcal{M}(+\infty)$, we obtain

$$A \simeq B \simeq \frac{\mathcal{M}(-\infty)}{2} \simeq \frac{\mathcal{M}_0}{2}. \quad (17)$$

In this way, A is the semi-amplitude of the function $\mathcal{M}(t)$ and it is approximately equal to half of the initial mass. In addition, B represents a vertical shift (roughly equal to A) which measures how far from $y = 0$ the asymptote is when $t \rightarrow +\infty$. On the other hand, κ is a coefficient measuring the ratio of mass-loss to mass squared, which according to the model remains constant along the atmospheric trajectory. It plays a similar role to that of the ablation coefficient in the equation (10).

Regarding times that define the maximum ablation regime, from the second derivative of equation (15), we obtain the time at which the mass-loss is maximum

$$t_{\max} = -\frac{C}{\kappa B^2}. \quad (18)$$

Analogously, from the third derivative, we obtain the times at the beginning and end of the interval in which the mass-loss is most severe. As a consequence of this model, the mass-loss would be symmetrical with respect to the time of maximum mass-loss.

We observe that the mass of the meteoroid can, thus, be parametrized by a generalized hyperbolic tangent function of time assuming the above-described model. Their parameters have been obtained from a non-linear least-squares minimization. Thus, we define the difference between the masses derived from equation (10) and those estimated from the model (15) as

$$N_i(t_i, \kappa, A, B, C) = M(t_i) - \mathcal{M}(t_i), \quad \text{with } i = 1, 2, \dots, n, \quad (19)$$

where t_i is the time for each observation i and n is the total number of observations.

Hence, we define the objective function

$$P : \mathbb{R}^4 \longrightarrow \mathbb{R}$$

$$(\kappa, A, B, C) \longmapsto P(\kappa, A, B, C) = \sum_{i=1}^n [N_i(t_i, \kappa, A, B, C)]^2. \quad (20)$$

Thus, we have to find the solution of the constrained problem given by

$$\begin{aligned} & \text{minimize } P(\kappa, A, B, C) \\ & (\kappa, A, B, C) \in \mathbb{R}^4 \\ & \text{subject to } \kappa < 0, A > 0, B > 0, \mathcal{M}(t_f) \geq 0, \end{aligned} \quad (21)$$

Table 5. Parameters of the mathematical model describing the Traspenna meteoroid mass-loss as it passes through the Earth’s atmosphere together with the times defining the maximum ablation regime.

Model parameters		
κ (kg ⁻¹ s ⁻¹)	$(-1.059 \pm 0.060) \times 10^{-3}$	
A (kg)	1307 ± 13	
B (kg)	1299 ± 12	
C (kg)	4907 ± 321	
Maximum ablation regime		
Time	Mass-loss	
t_{beg} (s)	\mathcal{M}_{beg} (kg s ⁻¹)	$(-1.21 \pm 0.48) \times 10^3$
t_{max} (s)	\mathcal{M}_{max} (kg s ⁻¹)	$(-1.81 \pm 0.10) \times 10^3$
t_{end} (s)	\mathcal{M}_{end} (kg s ⁻¹)	$(-1.21 \pm 0.46) \times 10^3$

where in order to avoid a meaningless result for the final mass $M(t_f)$, we impose the constraint that this must be non-negative. If we did not have measurements of the initial part of the bolide, we could also impose an analogous constraint on the initial mass. However, in the case of Traspenna, there are accurate measurements from the very beginning of the bolide and therefore this is not necessary.

Again, we search the optimal solution in the same way described in Section 3.1. In this case, differential evolution has proven to be the best choice. The adjusted coefficient of determination was $R^2 = 0.99938$. Parameters of the model as well as times and mass-loss values related to the maximum ablation regime are listed in Table 5.

Furthermore, taking into account the physical interpretation of the model parameters, we can give an approximate formula for the mass in terms of just three fundamental constants of the problem, namely the initial mass \mathcal{M}_0 , the mass-loss coefficient κ and the time of maximum ablation t_{max} , according to

$$\mathcal{M}(t) \simeq \frac{1}{2} \mathcal{M}_0 \left(1 + \tanh \left[\frac{1}{2} \mathcal{M}_0 \kappa (t - t_{\text{max}}) \right] \right), \quad t \in [t_0, t_f], \quad (22)$$

where t_0 and t_f are the beginning and ending times, respectively, of the fireball. The average accuracy of this approximation compared to that obtained with equation (15) is estimated using the mean value theorem for integrals in ± 7 kg.

One of the most important advantages of the proposed model is its ability to provide the time interval during which the meteoroid experienced the maximum ablation regime, as well as the time at which the mass-loss was maximum. The latter occurred 2.75 s after the onset of the fireball, in perfect agreement with the time of the first large flare, at 2.76 s. At that instant, the mass-loss was 1.81×10^3 kg s⁻¹. Furthermore, the times at which the mass-loss began to accelerate and decelerate occurred at 2.27 and 3.22 s, respectively, indicating that the most severe mass-loss would have occurred in that interval and also suggesting the occurrence of the most important fragmentation events. As shown in Fig. 9, this occurred while the meteoroid was descending from 42 to 29 km of height at a velocity of approximately 14 km s⁻¹. As a result, it lost 50 per cent of its mass in less than a second.

This four-parameter model suggests that the continuous ablation of the meteoroid is driven by a mass-loss law that initially leads to an exponential acceleration of the mass-loss followed by an exponential deceleration. In this regard, it would be interesting to apply it to other well-documented fireballs and verify if the hypothesis formulated about the mass-loss of the meteoroid due to ablation when passing through the Earth’s atmosphere, as shown in equation (14), is also

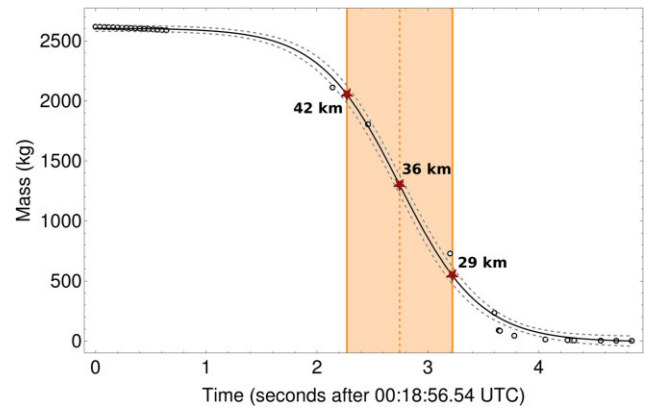


Figure 9. Mass depending on time derived from the mathematical model given in equation (15) is shown by means of the black curve. Confidence bands at 1σ are plotted as well. The shaded area between the two thick orange lines corresponds to the time interval when the mass-loss, and therefore the ablation, was most severe, i.e. between 2.27 and 3.22 s from the beginning. In addition, the time of maximum mass-loss, at 2.75 s, is indicated by a dashed orange line. The meteoroid velocity during this interval was approximately 14 km s⁻¹. Orthometric heights are shown for these times.

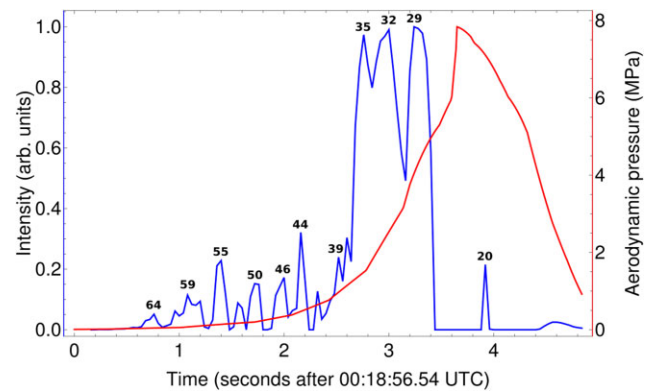


Figure 10. Superbolide uncalibrated light intensity (in arbitrary units) as a function of time obtained from the video recorded at the EPSE station (units are shown in the left vertical axis). Note that total values are normalized to the value at the peak and a linear scale is used to accentuate smaller features in the light curve. In addition, orthometric heights in kilometres are shown for the main flares listed in Table 6. The aerodynamic pressure curve derived using the velocity fit is plotted in red (units are shown in the right vertical axis).

true in other cases, at least in those of moderate-sized meteoroids or small asteroids like Traspenna.

3.7 Fragmentation model

We have obtained an uncalibrated light intensity curve of the superbolide (see Fig. 10) using the photometry of the video recorded at the EPSE station. Thus, despite the existence of fog, we were able to accurately determine the times corresponding to the main intensity peaks and even to roughly estimate their relative intensities. Nevertheless, as we do not have a model of light scattering and extinction due to the fog for this camera, we could not calibrate data and thus determine with enough confidence the variation of the absolute magnitude in time.

An analysis of the light curve reveals, however, a very regular flickering in the first part of the bolide that lasts until the onset of

the main flares. According to the interpretation of Beech & Brown (2000), this quasi-periodic brightness oscillations could be due to the rotation of an aspherical meteoroid. Anyhow, we cannot discard other effects like instabilities in evaporation, erosion or fast chemical reactions, although the most probable mechanism appears to be the successive detachment of fragments (wreckages) of lesser mass in comparison with the total meteoroid mass.

Since we do not have a calibrated light curve with a high time resolution that would allow us to fit a semi-empirical fragmentation model as, e.g. that of Borovička et al. (2013a), we have adopted a discrete fragment approach considering the main flares on the uncalibrated light curve and assuming that at least the most bright of them represent discrete fragmentation events. Accordingly, the meteoroid would have disintegrated into fragments that would have continued their flights as independent bodies and could have undergone further disintegrations. As a matter of fact, the uncalibrated light curve shows strong evidence for a significant fragmentation of the meteoroid and, indeed, a trail of nine fragments (labelled A–I) was recorded from Corullón. This can be easily discerned in the expanded view of the frame obtained just 0.64 s before the end of the bolide (see Fig. 11). These fragments would be the result of the three main fragmentation events that occurred between 35 and 29 km of height that can be distinguished, albeit with difficulty, in the Nigrán video (unfortunately, they are outside the fields of view of those of Corullón, Ponferrada, and Caldas de Reis). Hence, the sudden rise in the bolide brightness could easily be explained by the increase in the total surface area of the meteoroid after each fragmentation.

In fact, just after each fragmentation, the meteoroid fragments fly as a unit within a single bow shock until they are separated enough to have individual bow shocks. At this point, high pressures are generated that produce a transverse acceleration of the meteoroid trajectory and thus, a transverse velocity of repulsion that is given by the formula of Passey & Melosh (1980)

$$v_T = \left(\frac{3}{2} C_R \frac{r_1 \rho_a}{r_2 \rho_m} \right)^{\frac{1}{2}} v, \quad (23)$$

where C_R is the coefficient of repulsion, being $C_R \approx 1$ the most probable value according to the authors, although it would be 0.2 for two equal fragments, as stated by Artem'eva & Shuvalov (1996); r_1 and r_2 are the radii of the fragments; ρ_a and ρ_m are the atmospheric density and the meteoroid density, respectively; and v is the meteoroid velocity along the trajectory. On the other hand, the fact that the meteoroid broke into small fragments of similar size could be explained, in agreement with the mechanism proposed by Tabetah & Melosh (2018), if the permeability and porosity of the meteoroid were low. In this case, lateral velocities may appear after the disruption of the meteoroid leading to an increase of the scattering field although probably not too large.

Nevertheless, Schultz & Sugita (1994) showed that the interacting shocks act not to disperse but to collimate the fragments below a critical size which depends on the transverse velocity and atmospheric density. In addition, collimation of the entire debris cloud within a Mach cone acts to minimize the drag coefficient and thus reduce deceleration. This requires, however, that the transverse velocity of repulsion be small compared to the meteoroid velocity along the trajectory. Estimates of the transverse velocity at each fragmentation event for the Traspesa meteoroid are shown in Table 6. Since these velocities are, indeed, very small in comparison with the meteoroid velocity, 20 m s^{-1} at most during the main flares, this phenomenon could explain the low height reached by the fragmented meteoroid in the case of Traspesa.

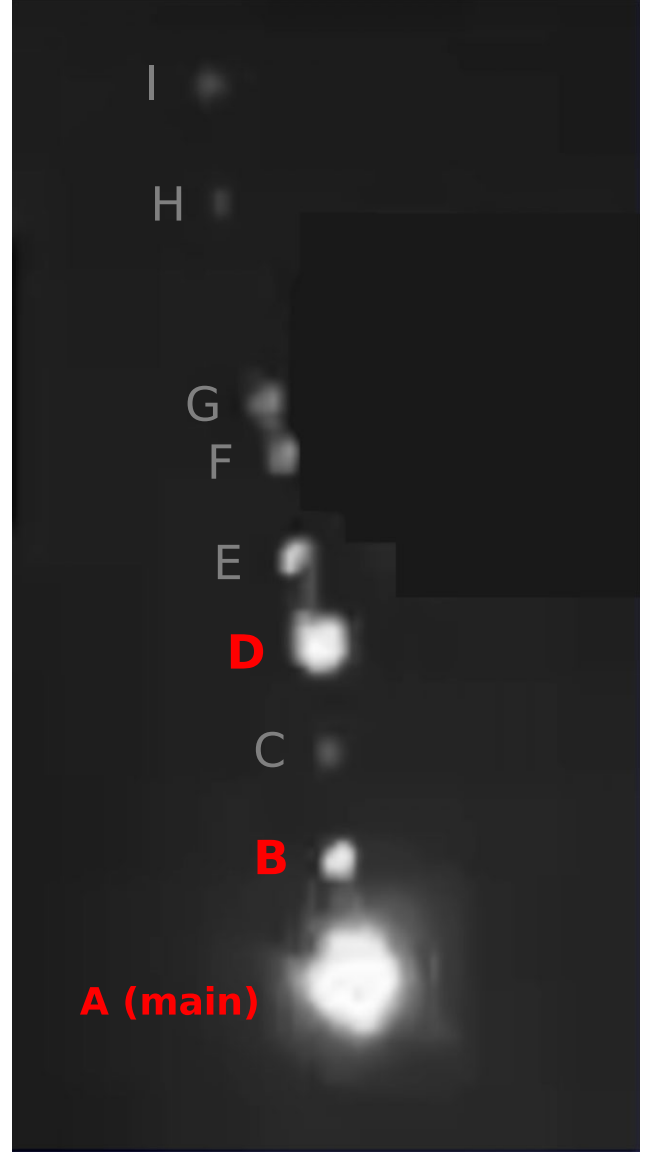


Figure 11. Snapshot of the bolide extracted from the casual video obtained from Corullón, at a range of 54.8 km, just 0.64 s before the end. Up to nine separate fragments are clearly shown (labelled A–I). All of them are spread over a distance along the trajectory of roughly 8 km and the height of the main body is 17.74 km at this time. The largest fragments, for which independent astrometric measurements exist, are shown in red.

On the other hand, fragmentation of the meteoroid occurs when the aerodynamic pressure is

$$P = \frac{c_d}{2} \rho_a v^2, \quad (24)$$

where c_d is the drag coefficient, ρ_a is the atmospheric density, and v is the actual velocity of the meteoroid, exceeding the mechanical strength of the meteoroid material. Large bodies can therefore break into smaller fragments. The tiniest of these fragments as well as those produced by spallation will eventually be vaporized, but some others will survive to reach the ground as meteorites. The maximum aerodynamic pressure, 7.84 MPa, was reached when the meteoroid, still with a total mass of roughly 85 kg, had a velocity of 11.04 km s^{-1} , at a height of 21.47 km. The expected aerodynamic pressures at the times when flares were observed are listed as well in Table 6.

Table 6. Main features of the flares observed in the Traspenna superbolide: time since the beginning of the superbolide, normalized intensity (uncalibrated), orthometric height, meteoroid velocity, transverse velocity of repulsion, and aerodynamic pressure. Times of the most outstanding ones are highlighted in bold. Note that the time of the maximum aerodynamic pressure and their associate data are shown between parentheses.

t (s)	I	H (km)	v (km s ⁻¹)	v_T (m s ⁻¹)	P (MPa)
0.76	0.1	63.61	15.06 ± 0.10	2.1	0.0446 ± 0.0006
1.08	0.1	59.08	15.04 ± 0.10	2.7	0.0736 ± 0.0010
1.40	0.2	54.55	15.01 ± 0.10	3.8	0.1408 ± 0.0018
1.56	0.1	52.29	14.99 ± 0.10	4.2	0.1719 ± 0.0023
1.72	0.2	50.02	14.97 ± 0.10	4.5	0.2013 ± 0.0027
2.00	0.2	46.06	14.90 ± 0.10	5.9	0.3442 ± 0.0047
2.16	0.3	43.80	14.84 ± 0.11	6.9	0.4737 ± 0.0068
2.52	0.2	38.71	14.65 ± 0.12	9.9	0.975 ± 0.016
2.76	1.0	35.32	14.43 ± 0.13	12	1.517 ± 0.027
3.00	1.0	31.94	14.10 ± 0.14	16	2.581 ± 0.052
3.24	1.0	28.54	13.61 ± 0.15	20	4.123 ± 0.092
(3.65)	–	(21.47)	(11.04 ± 0.16)	–	(7.84 ± 0.23)
3.92	0.2	19.58	9.08 ± 0.16	17	7.11 ± 0.25
4.56	0.0	16.59	4.42 ± 0.18	28	2.77 ± 0.23

Therefore, the process of disintegration of a body during atmospheric braking can be viewed as a chain of successive fragmentations of the meteoroid, separated in space and time, into a number of comparable size chunks. Hence, progressively smaller and smaller fragments are produced as aerodynamic drag increases. In fact, it is reasonable to assume that as the load increases to its maximum value, each fragment is successively split in two.

The uncalibrated light curve (see Fig. 10) shows many fluctuations between 0.7 and 2.2 s (above 43 km of height) suggesting that the meteoroid underwent a number of small fragmentations during its flight. These would have occurred at aerodynamic pressures below 0.5 Mpa. Moreover, wakes are clearly observed in the first frames of one of the Caldas de Reis video recordings (at 0.68 s from the beginning) and in that of the Nigrán video recording (at 1.62 s from the beginning). In fact, the formation of wakes would be evidence, in agreement with Shrbený, Spurný & Borovička (2020), that fragmentation was in progress shortly after the onset. However, neither the release of dust in the wake of the small fragments nor irregular erosions due to the rotation of the meteoroid can be ruled out. Actually, we can suppose a quasi-continuous fragmentation in the form of eroded dust along the entire length of the bolide.

Therefore, the fragmentation would have split the bolide into a number of smaller fragments, as well as a cloud of debris of lower mass. In fact, three very bright flares caused by large fragmentation events are observed between 2.76 and 3.24 s. The main fragmentations would have occurred between aerodynamic pressures of 1.5 and 4.2 MPa, in agreement with the values observed for a meteoroid with enough mass to reach dense atmospheric layers with a relatively large velocity. This suggests that the parent asteroid of the Traspenna meteorite would have been an object with a consistency similar to those of the other ordinary chondrites. In fact, according to Popova et al. (2011), meteoroids like Traspenna, with sizes on the order of a metre, are often highly fractured before entry and can break under stresses of a few megapascals.

These large fragmentation events resulted in two additional smaller fireballs (D and B in Fig. 11) for which, remarkably, it was possible to obtain sufficiently accurate astrometric measurements to calculate their trajectories as single bodies. Furthermore, we have parametrized

Table 7. Steps in the procedure followed to derive reliable final masses for each fragment.

Steps	Mass (kg)		
	A	D	B
First : single-body model	1.920	0.249	0.345
Second: mass correction procedure	0.92	0.25	0.14
Actual values	0.527	Not found	Not found

their atmospheric flights using the dimensionless coefficient method (described in Section 3.3 for the main body) which, as far as we know, is the first time this has been done for secondary fragments. As a result, individual masses were obtained for each fragment after deriving their ballistic and mass-loss parameters. Finally, a correction procedure to estimate the remaining mass of each body taking into account the major fragmentation events was accomplished applying equation (10) jointly to each of them (see Table 7).

We note that there is an excess of mass between the estimated mass for the main body, 0.92 kg, and the mass of the recovered meteorite, 0.527 kg. This excess of mass can be explained taking into consideration that the single-body model has been applied assuming that the original meteoroid underwent only two large fragmentations when most probably there were a few more, as can be deduced from Fig. 11, where eight fragments are observed in addition to the main body. We believe that this 0.39 kg would be, in fact, the mass corresponding to smaller fragments for which astrometric measurements are not available. This would not necessarily imply that any of these smaller fragments survived the ablation process and landed, but most likely that at least a significant fraction of this mass was vaporized before the dark flight began.

Therefore, the first conspicuous fragmentation occurred at a height of 35.32 km at 2.76 s from the beginning, under an aerodynamic pressure of 1.517 MPa, when a 406-kg fragment detached from the main body. This was followed by an outstanding flare, when the superbolide reached its maximum brightness, produced by other major fragmentation at 28.54 km of height under an aerodynamic pressure of 4.123 MPa. At that moment, 3.24 s after the start of the bolide, a 114 kg fragment separated from the main body which continued its trajectory with a mass of 286 kg. Below this height, the bolide brightness decreased very steeply and only a last bright flare was observed 0.92 s before the final, at 19.58 km of height. As usual, the deceleration of the meteoroid in the last part of its trajectory was faster than expected due to fragmentation.

Finally, the two largest fragments of the trail faded gradually. The leading main body A reached 15.75 km final height whereas the brilliant fragments, D and B, faded completely at 19.01 and 18.71 km, respectively. Subsequently, these individual pieces of the fragmented meteoroid were intensely decelerated until thermal ablation ceased and the surviving fragments continued their dark flights until they hit the ground. The two major fragmentation events are shown in Fig. 12.

4 THE METEORITE FALL

4.1 The dark flight modelling

The meteoroid decelerated to a velocity as low as 2.38 km s⁻¹ at the end of the luminous trajectory. We can suppose this low velocity corresponds roughly to that at which the ablation process stopped. The dark flight calculations were performed assuming that the fragments followed individual ballistic trajectories under the Earth's

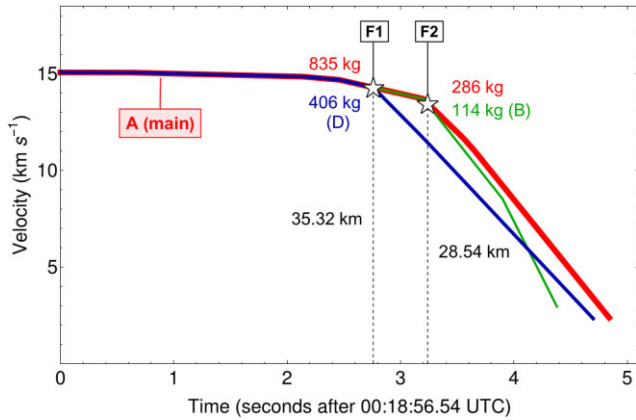


Figure 12. Schematic representation of the two major fragmentation events (F1 and F2) in the velocity versus time diagram. The masses of the main body after each fragmentation are shown in red while those corresponding to fragments D and B are shown in blue and green, respectively.

gravity and influenced by air drag and atmospheric winds but keeping their masses constant.

The expected impact points of the meteorites after their dark flights were calculated using the method of Ceplecha (1987) which accounts for atmospheric drag, winds, and Earth’s rotation. It needs the position, velocity, and deceleration of each fragment at the moment of ablation stop together with the wind vertical profile. As the author of the method himself pointed out, the most serious problems in this calculation are the lack of knowledge about the winds in the region of the event and the unknown shape of the meteoroid. Regarding the latter, we assume that the shape of each of the fragments is spherical as the actual shape is not known. More critical is the question of the winds during the dark flight since there is considerable uncertainty about them.

The only available meteorological data were obtained with a radiosonde launched by the *Agencia Estatal de Meteorología* (AEMET) from A Coruña, a maritime city 120 km away from the fireball, about 20 min before the fireball. According to that, strong winds of about 35 m s^{-1} were encountered at heights of about 25 km flowing with a westerly direction. Between 15 and 5 km, the winds were generally from the NE with an average velocity of 10 m s^{-1} ; at lower heights, dominant wind was from NW with constant velocities around 5 m s^{-1} (see Fig. 13). Therefore, the fall of meteorites must have been significantly influenced by northeasterly winds.

The equations of motion which define the dark flight were integrated considering a novel aerodynamic model fully depending on the actual atmospheric conditions as functions of height. Moreover, the drag coefficient c_d was calculated using the equation of Carter, Jandir & Kress (2009) for a sphere. This is strongly dependent on the Mach number, which in turn was calculated as a function of height and temperature. In this case, the drag coefficient reached its maximum at 13.81 km of height and decreased steeply to about 13 km of height. Thereafter, it continued to decrease smoothly as shown in Fig. 14. As a matter of fact, at the beginning of the dark flight at a height of 15.75 km, the meteoroid still was moving in a hypersonic regime. However, it quickly became subsonic at 14.42 km of height when according to our atmospheric model the speed of sound was 289 m s^{-1} .

In addition, gravity depending on height was also integrated in the model considering the parameters of the GRS80. Finally, the Coriolis force, despite being a small contribution, was also taken into account. The integration of the model equations was carried out

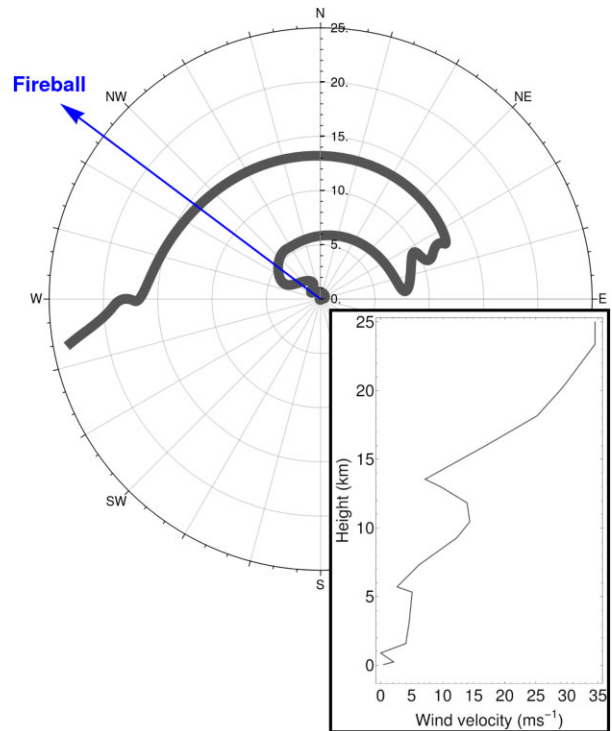


Figure 13. Wind vertical profile derived from measurements of the radiosonde launched by the AEMET in A Coruña (located at about 120-km away from the fireball) at 00:00 UTC on 2021 January 18. The polar plot shows wind direction depending on height (in kilometres). The blue arrow indicates the fireball motion direction on the ground whereas the rectangular plot on the right bottom corner shows wind velocity depending on height.

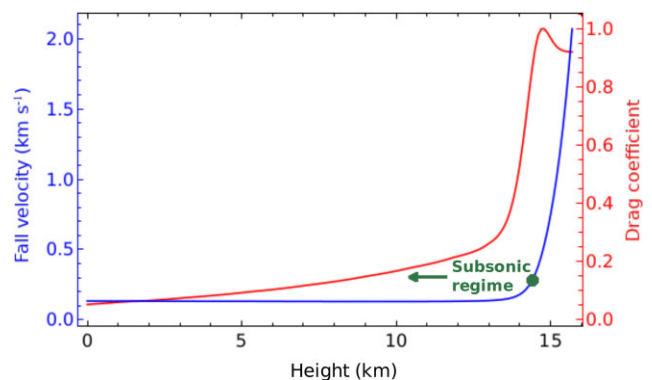


Figure 14. Drag coefficient c_d depending on height considering a spherical shape and taking into account the actual atmospheric conditions experienced by the Traspenna meteorite during the dark flight is shown in red whereas the velocity fall is shown in blue. The green disc indicates the point at which the meteorite entered the subsonic regime at a height of 14.42 km. This continued until it reached a terminal velocity of 134 m s^{-1} .

using an eighth-order explicit Runge–Kutta integrator with adaptive step-size control for error handling.

As a result, the main body underwent a small longitudinal shift of only -38 m (that is, a backward movement in the direction of motion) but a noticeable lateral shift of -498 m (i.e. to the left as viewed from the position of the body facing in the direction of motion) as shown in Fig. 15.

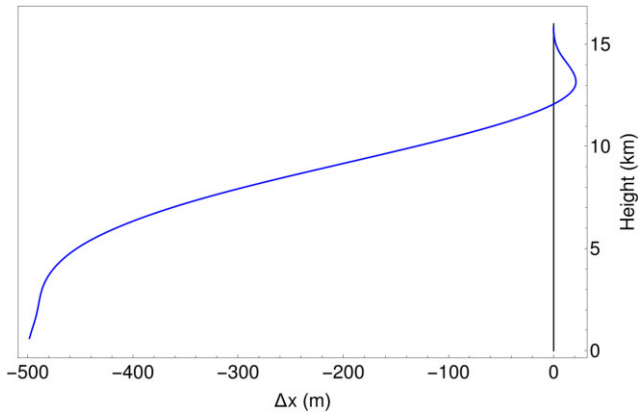


Figure 15. Lateral shift of the Traspenna meteorite (main body) due to the wind during the dark flight. The vertical line shows the vertical path of the body without lateral winds. Note that both axes are not in the same scale.

4.2 Computing the strewn field

Each fragment of the original meteoroid that survived the ablation phase during the atmospheric trajectory would have impacted on the ground at different locations depending on its shape and, above all, on the atmospheric winds blowing during its dark flight. In fact, parameters obtained in Section 3.7 for each fragment, all of them referred to the main-body atmospheric trajectory given in Section 3.1, have allowed to model the dark flight of each individual fragment as completely independent bodies and, thus, computing the strewn field much more accurately. In this way, the dark flight model has been applied not only to the main body but also to fragments D and B produced in the two major fragmentation events (see Fig. 12).

To account for the wind variability, we have used Monte Carlo simulations assuming that both the zonal and the meridional components of the wind velocity are normally distributed around their nominal values at each height step. Thus, the equations of the model described in Section 4.1 have been integrated for each fragment taking random values of the wind components within a 20 per cent of variability assuming a Gaussian distribution. Each integration has been repeated taking new values of the wind components until 10^4 simulations were completed.

Results concerning the dark flight of each fragment are given in Table 8 and the strewn field is shown in Fig. 16. We observe that, as expected, the effect of the winds has been somewhat different depending on the height at which each fragment was released. Thus, fragments D and B compared to the main body A have undergone a larger deceleration in the longitudinal direction but a smaller lateral

shift. Note that the region of fall of potential meteorites is unusually small because of the steep trajectory in the atmosphere.

We would like to emphasize that our model does not assume a priori that the main body corresponds to the recovered meteorite and that this conclusion is indeed a natural result of its application. As a matter of fact, the accurate atmospheric trajectory calculated in Section 3.1 and the dynamics provided by the fine tuning of velocities given in Section 3.2 are the two factors that constrain the initial values that determine the dark flight of each fragment.

On the other hand, we have estimated the mass distribution of fragments using the power-law mass frequency distribution given by Brykina & Egorova (2021) to obtain the cumulative number of fragments

$$N_m = \frac{1 - \delta}{\delta l^{1-\delta}} \left[\left(\frac{m_f}{M_t} \right)^{-\delta} - l^{-\delta} \right] + n_l, \quad (25)$$

being m_f the fragment mass, M_t the total mass of all fragments, n_l the number of fragments with the largest mass m_l , and $l = m_l/M_t$, the dimensionless fragment mass. The power index, $0 < \delta < 1$, takes typical values between 0.5 and 0.7 for rocks suffering a single impact.

In this case, in agreement with the results shown in Table 8, we have taken the largest mass as that of the main body A weighing 0.527 kg and have fitted equation (25) to the masses derived in Section 3.7 for each hypothetical fragment D and B. Thus, we have derived a power index $\delta = 0.5825$ for the fragmentation of the Traspenna meteoroid. According to that, we could expect to find at least two meteorites of 0.25 and 0.14 kg that we could identify with fragments D and B, respectively, in Fig. 11. We cannot rule out, however, that there are still smaller meteorites than those (which would have been produced in some of the small fragmentations) but, in any case, we expect their masses to be distributed as shown in Fig. 17. However, considering that these small fireballs have been extinguished at higher heights and that likely their masses were small, this does not seem the most likely outcome.

4.3 Searching meteorites

A search group coordinated from the *Escola Politécnica Superior de Enxeñaría* (EPSE–USC) at the city of Lugo, located about 20 km north-west of the predicted fall site and formed basically by members of the USC has been looking for possible meteorites in the region for a considerable period since late January 2021.

Unfortunately for us, the terrain conditions and the orography of the region worked against our objective. Indeed, the entire area of probable fall is located in the foothills of the Os Ancares mountains and most of the terrain is heavily vegetated, alternating with some

Table 8. The dark flight of the Traspenna meteorite (main body) along with the expected dark flights of two smaller fragments. Geodetic coordinates are referenced to the GRS80 (\approx WGS84) ellipsoid. We note that the main body was recovered at only 31 m from the expected impact point on the ground. Actual location and mass are shown for the recovered meteorite.

		A (main body: recovered)	D	B
Latitude ($^\circ$)	φ_m	42.87133 (actual: 42.87112)	42.86592	42.86606
Longitude ($^\circ$)	λ_m	-7.3228 (actual: -7.3230)	-7.3113	-7.3120
Longitudinal shift (m)	Δl_m	+782	+469	+445
Longitudinal shift (only wind) (m)	Δl_m	-40	-412	-389
Lateral shift (m)	Δx_m	-499	-192	-222
Time of flight (s)	Δt_m	105	131	131
Impact velocity (m s^{-1})	v_m	134	132	131
Final mass (kg)	M_m	0.92 (actual: 0.527)	0.25	0.14

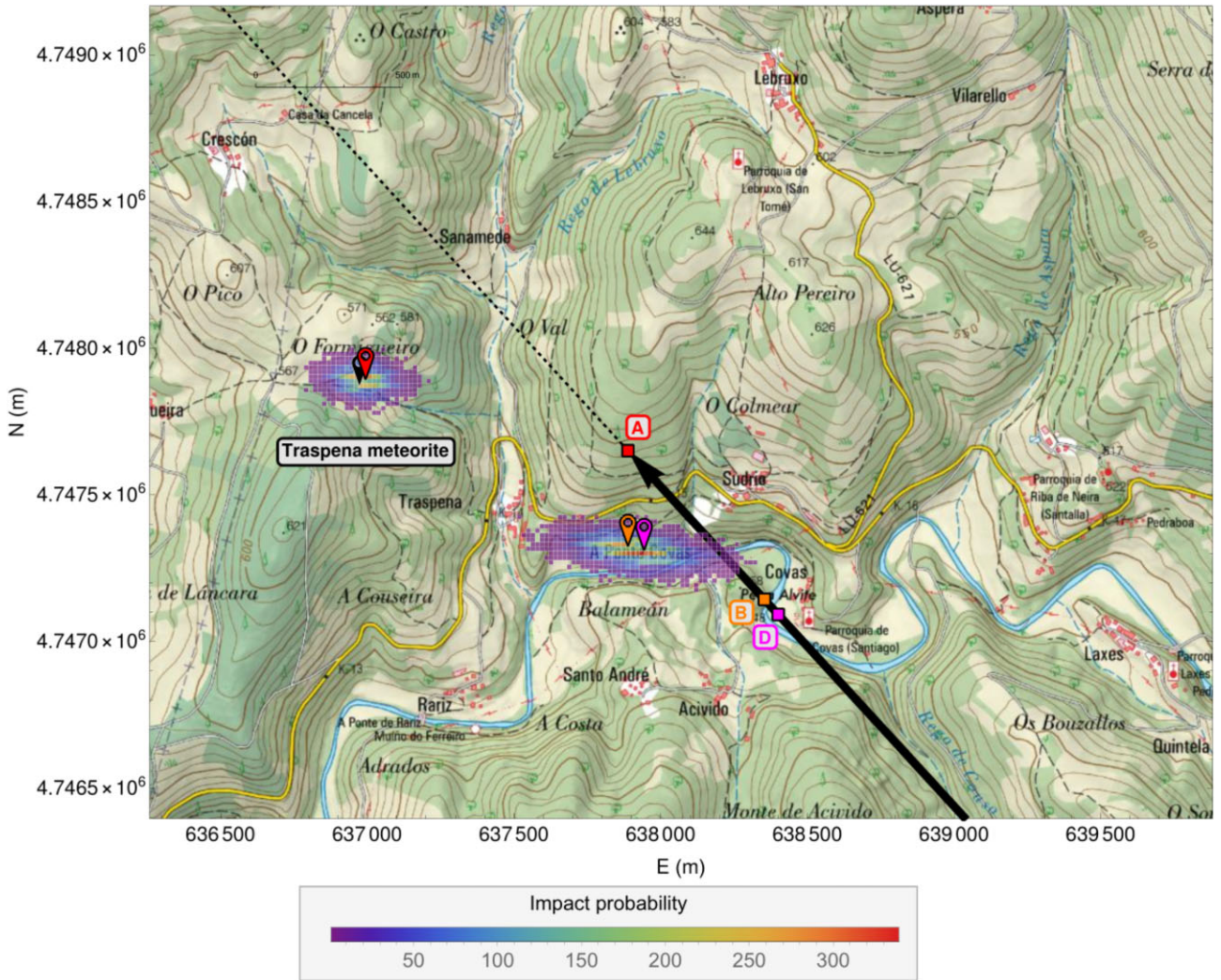


Figure 16. The Traspena strewn field with the predicted impact area for meteorites (map source: IGN; CRS: ETRS89–TM29). The actual position of the sole recovered meteorite A is indicated with a black drop icon whereas its calculated impact position (both separated only 31 m) is marked with a red drop icon. In addition, calculated impact positions of possible fragments D and B are marked with magenta and orange drop icons, respectively. Locations on the atmospheric trajectory where each fragment was released are shown with coloured squares using the same legends. The bottom bar shows the probability computed using 10^4 Monte Carlo simulations with a variability in the speed of winds of 20 per cent. The ground projection of the atmospheric trajectory is shown using a solid black line whereas the dashed line indicates the dark flight (without atmosphere).

grazing areas for cattle. In addition, in the spring and summer months, we had to be very careful with ticks which are endemic transmitters of dangerous diseases in this region.

Nevertheless, our main drawback in finding the meteorite was that we did not have reliable calibrations of some of the most relevant videos, necessary to calculate an accurate solution for the atmospheric trajectory until a few months after the fall. During this time we interviewed dozens of people and explained to them the scientific importance of recovering meteorites.

In this regard, another of the most serious problems we had to face, which unfortunately arises every time a meteorite falls, was the arrival of meteorite hunters who led local people to become wary of giving information and even of reporting possible recoveries. Thus, in the space of a few weeks we could see that the initial scientific curiosity of many locals about this event had sadly been replaced by greed at the real possibility that one of them could find a meteorite and sell it for a considerable sum of money to any of the meteorite hunters. That is why we encourage our scientific colleagues to not

collaborate with these meteorite hunters whose only aim is to plunder a geological heritage that, as in other countries, is also protected by law in Spain. We could thus prevent these fascinating objects of the cosmos from ending up in the hands of private collectors instead of in public scientific museums where we can all enjoy them.

4.4 The recovered meteorite

The inhabitants of western Baralla and eastern Láncara knew soon after the fall that several search groups were looking for meteorites in the surroundings. We ourselves were constantly talking to them to find out if they had seen any *rare* stone.

Finally, a local resident, Jesús Ángel Farelo, who already knew that there were searches in progress in the area, would find an ordinary chondrite by chance on 18 March close to a dirt track in a meadow of his family where he usually takes his cattle to graze. This property is called O Formigueiro and it is located in the small village of Traspena, in the parish of Covas (Baralla), close

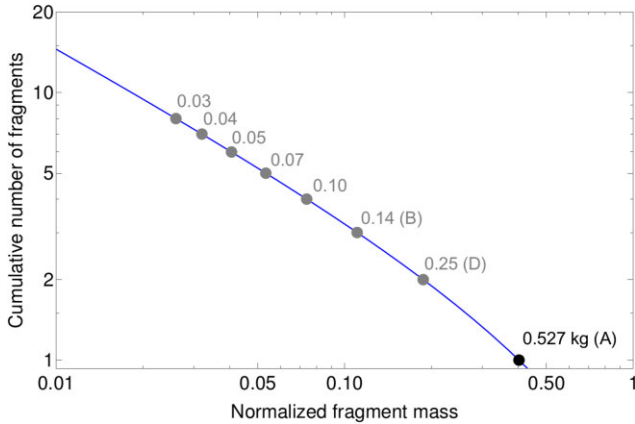


Figure 17. Cumulative number of fragments as a function of the normalized fragment mass with the power index in equation (25) equal to $\delta = 0.5825$. The recovered meteorite is shown in black in the bottom part of the plot, while fragments that might eventually still be found, together with their masses in kilograms, are shown in grey.

to the river Neira, at geodetic coordinates $\lambda = -7^\circ 19' 22.94''$ and $\varphi = 42^\circ 52' 16.05''$. Astonishingly, this same person had walked this path on other occasions since the fall but it was not until that day that he found it. However, because of the suspicions that the meteorite hunters had raised, this person decided not to make the find public and to discreetly look for a geologist he trusted who could analyse the meteorite, so he eventually passed it on to one of us (JG-G).

The recovered meteorite exhibited a rounded brick shape of approximately $9 \times 7 \times 5$ cm and weighed 527.0 ± 0.1 g. A bulk density of 3.25 ± 0.01 g cm $^{-3}$ was measured. After 2 month outdoors, the fusion crust showed some tiny rust marks. There were no traces of impact except for a small nick in one corner. It is quite possible that it had fallen several tens of metres further up the ground (to the north), as the terrain has a moderate slope, and that the rain and the passage of the cattle during the last 2 month of winter had dragged it down the hillside to where it finally appeared (see Fig. 18). In fact, inner sections exhibit brownish areas of iron oxides towards the periphery and a less oxidized core, i.e. a pattern of weathering traces scarcely observed in chondrites which may be due to its 2 month of terrestrial lying on a damp bed.

The middle part of the only recovered fragment was cut into small sections for physical and geochemical study at the *Museo Nacional de Ciencias Naturales* (MNCN-CSIC, Madrid), the *Institut de Ciències de l'Espai* (ICE-CSIC, Barcelona), and the *Universitat Politècnica de Catalunya* (Barcelona), where 29, 24, and 18 g, respectively, are currently deposited.

The smaller of the two remaining pieces, weighing 182 g, was given to the local council of Baralla by the finder of the meteorite. The main piece, weighing 202 g, was acquired by the *Museo de Historia Natural* of the USC (MHN-USC) in order to ensure its preservation for future generations and to have it permanently on public display.

5 DYNAMICS OF THE PARENT ASTEROID

5.1 The heliocentric orbit

At present, there are only a few tens of recovered meteorites with accurate heliocentric orbits computed from reliable observations of a fireball as shown in Table 9.



Figure 18. Background photography (by Jesús Ángel Farello): Traspenna meteorite as found by Jesús Ángel Farello. It was close to a dirt track in a meadow of his family in O Formigueiro (Traspenna, Covas, Baralla). Fore-ground photography: this ordinary chondrite exhibits several regmaglypts.

The pre-entry heliocentric orbit was analytically computed from the known radiant, the pre-atmospheric velocity, and the bolide time using the method of Ceplecha (1987), therefore assuming an initial hyperbolic collision orbit with Earth. This is also the same method that has been implemented in other recent orbit calculators, which in fact basically reproduce the results obtained here, e.g. Peña-Asensio et al. (2021), but with some particularities that we comment below that make the software developed at the EPSE-USC highly accurate.

We note that the velocity before atmospheric entry is not assumed to be the velocity of the meteor at the beginning of its luminous phase (see Section 3.2) since we cannot neglect deceleration before the starting of the thermal ablation. The zenith attraction correction was applied using the Schiaparelli scheme with the Andreev (1991) approach at the beginning point of the trajectory. On the other hand, since the ECI coordinates of the stations were moving with time when the trajectory was calculated, the radiant does not need to be corrected for the Earth's rotation. However, since the ECI coordinates of the meteor are in the epoch of the date, they must be precessed to J2000. Regarding the Cartesian heliocentric ecliptic coordinates of the Earth, these were directly computed using the JPL DE441 ephemerides (Park et al. 2021) for the beginning of the bolide on the TDB time-scale. Uncertainties have been derived using the Monte Carlo approach described in Section 3.1.

The geocentric radiant and the geocentric velocity together with the orbital elements (referred to the J2000 equinox) are listed in Table 10 and the heliocentric orbit is shown in Fig. 19.

Table 9. List of meteorites (sorted by date of fall) whose recovery was accompanied by the necessary observational information to ensure a sufficiently accurate calculation of the heliocentric orbit. The official name of the meteorite, fall date, type, mass of the meteoroid before atmospheric entry and recovered mass, are given in the second to fifth columns, respectively. In addition, semimajor axis, eccentricity, inclination, and orbital type are shown in the sixth to ninth columns, respectively. The main reference for the published heliocentric orbit is given in the last column.

N^a	Name	Date (UTC)	Type	M_e M (kg)	a (au)	e	i (°)	Orbit	Reference
1	Příbram	07/04/1959	H5	<5000 5.56	2.424	0.6742	10.4244	Apollo	Ceplecha (1961)
2	Lost City	04/01/1970	H5	165 17	1.66	0.417	12.0	Apollo	McCrosky et al. (1971)
3	Innisfree	06/02/1977	L5	42 4.58	1.872	0.4732	12.27	Apollo	Halliday, Blackwell & Griffin (1978)
4	Benešov	07/05/1991	LL3.5,H5	4100 0.01	2.483	0.6274	23.981	Apollo	Spurný et al. (2014)
5	Peekskill	09/10/1992	H6	<10000 12.57	1.49	0.41	4.9	Apollo	Brown et al. (1994)
6	Tagish Lake	18/01/2000	C2	75 10	1.98	0.55	2.0	Apollo	Hildebrand et al. (2006)
7	Morávka	06/05/2000	H5	1500 0.63	1.85	0.47	32.2	Apollo	Borovička et al. (2003)
8	Neuschwanstein	06/04/2002	EL6	300 6.19	2.40	0.670	11.41	Apollo	Spurný, Oberst & Heinlein (2003)
9	Park Forest	27/03/2003	L5	11 000 18	2.53	0.680	3.2	Apollo	Brown et al. (2004)
10	Villalbeto de la Peña	04/01/2004	L6	760 3.5	2.3	0.63	0.0	Apollo	Trigo-Rodríguez et al. (2006)
11	Bunburra Rockhole	20/07/2007	Eucrite	22 0.32	0.8529	0.2427	8.95	Aten	Spurný et al. (2012)
12	Almahata Sitta	07/10/2008	Ureilite	83 000 3.95	1.308201	0.312065	2.54220	Apollo	Jenniskens et al. (2009)
13	Buzzard Coulee	21/11/2008	H4	15 000 41	1.25	0.23	25.0	Apollo	Milley (2010)
14	Maribo	17/01/2009	CM2	1500 0.03	2.43	0.805	0.25	Apollo	Borovička, Popova & Spurný (2019)
15	Jesenice	09/04/2009	L6	170 3.67	1.75	0.431	9.6	Apollo	Spurný et al. (2010)
16	Grimsby	26/09/2009	H5	33 0.22	2.04	0.518	28.07	Apollo	Brown et al. (2011)
17	Košice	28/02/2010	H5	3500 4.3	2.71	0.647	2.0	Apollo	Borovička et al. (2013a)
18	Mason Gully	13/04/2010	H5	40 0.02	2.47	0.6023	0.832	Apollo	Spurný et al. (2011)
19	Križevci	04/02/2011	H6	62 0.29	1.544	0.521	0.64	Apollo	Borovička et al. (2015)
20	Sutter's Mill	22/04/2012	C	50 000 0.99	2.59	0.824	2.38	Apollo	Jenniskens et al. (2012)
21	Novato	18/10/2012	L6	80 0.31	2.09	0.526	5.51	Apollo	Jenniskens et al. (2014)
22	Chelyabinsk	15/02/2013	LL5	1.2×10^6 1000	1.72	0.571	4.98	Apollo	Borovička et al. (2013b)
23	Annama	18/04/2014	H5	472 0.17	1.99	0.69	14.65	Apollo	Trigo-Rodríguez et al. (2015)
24	Žd'ár nad Sázavou	09/12/2014	L3.9	170 0.05	2.093	0.6792	2.796	Apollo	Spurný, Borovička & Shrbený (2020)
25	Porangaba	09/01/2015	L4	0.976 –	2.54	0.64	8.6	Apollo	Ferus et al. (2020)
26	Sarıççek	02/09/2015	Howardite	13 000 15.24	1.44	0.301	22.6	Apollo	Unsalan et al. (2019)
27	Creston	23/10/2015	L6	55 0.688	1.300	0.410	4.288	Apollo	Jenniskens et al. (2019)
28	Murrili	27/11/2015	H5	– 1.68	2.521	0.609	3.32	Apollo	Sansom et al. (2020)
29	Osceola	24/01/2016	L6	>1800 1.099	1.486	0.3406	13.20	Apollo	Meier et al. (2020)
30	Ejby	06/02/2016	H5/6	250 8.94	2.81	0.655	0.96	Apollo	Spurný et al. (2017)
31	Stubenberg	06/03/2016	LL6	600 1.47	1.525	0.395	2.07	Apollo	Spurný et al. (2016)
32	Dishchii' bikoh	02/06/2016	LL7	9000 0.0795	1.129	0.205	21.24	Apollo	Jenniskens et al. (2020)
33	Dingle Dell	31/10/2016	L/LL5	40 1.15	2.254	0.5904	4.051	Apollo	Devillepoix et al. (2018)
34	Hamburg	17/01/2018	H4	142 1.0	2.73	0.661	0.604	Apollo	Brown et al. (2019)
35	Motopi Pan	02/06/2018	Howardite	5500 0.214	1.37640	0.431861	4.29741	Apollo	Jenniskens et al. (2021)
36	Ozerki	21/06/2018	L6	7 6.5	0.84	0.199	18.44	Aten	Kartashova et al. (2020)
37	Viñales	01/02/2019	L6	– 50	1.217	0.391	11.47	Apollo	Zuluaga et al. (2019)
38	Arpu Kuilpu	01/06/2019	H5	2.2 0.042	2.75	0.671	2.03	Apollo	Shober et al. (2022)
39	Flensburg	12/09/2019	C1	15 000 0.0245	2.82	0.701	6.82	Apollo	Borovička et al. (2021)
40	Cavezzo	01/01/2020	L5	3.5 0.055	1.82	0.460	4.0	Apollo	Gardiol et al. (2021)
41	Novo Mesto	28/02/2020	L5	470 0.72	1.451	0.60866	8.755	Apollo	Vida et al. (2021)
42	Madura Cave	19/06/2020	L5	64 1.072	0.889	0.327	0.12	Aten	Devillepoix et al. (2022)
43	Traspena	18/01/2021	L5	2620 0.527	1.125	0.386	4.55	Apollo	This paper

Note. ^a1: Central Bohemian Region (Czech Republic); 2: Oklahoma (USA); 3: Alberta (Canada); 4: Central Bohemian Region (Czech Republic); 5: New York (USA); 6: British Columbia (Canada); 7: Moravian–Silesian Region (Czech Republic); 8: Bavaria (Germany); 9: Illinois (USA); 10: Castile and León (Spain); 11: South Australia (Australia); 12: Northern State (Sudan); 13: Saskatchewan (Canada); 14: Region Zealand (Denmark); 15: Upper Carniola (Slovenia); 16: Ontario (Canada); 17: Košice Region (Slovakia); 18: Western Australia (Australia); 19: Koprivnica–Križevci County (Croatia); 20: California (USA); 21: California (USA); 22: Chelyabinsk Oblast (Russian Federation); 23: Murmansk Oblast (Russian Federation); 24: Vysočina Region (Czech Republic); 25: São Paulo (Brazil); 26: Bingöl (Turkey); 27: California (USA); 28: South Australia (Australia); 29: Florida (USA); 30: Capital Region of Denmark (Denmark); 31: Bavaria (Germany); 32: Arizona (USA); 33: Western Australia (Australia); 34: Michigan (USA); 35: Ghanzi (Botswana); 36: Lipetsk Oblast (Russian Federation); 37: Pinar del Río (Cuba); 38: South Australia (Australia); 39: Schleswig–Holstein (Germany); 40: Emilia–Romagna (Italy); 41: Lower Carniola (Slovenia); 42: Western Australia (Australia); 43: Galiza (Spain).

5.2 Looking for potential dynamic associations with NEOs

The orbital elements indicate that the parent asteroid of the Traspena meteorite was an object of the Apollo group of the near-Earth asteroids (NEAs) with moderate eccentricity, low inclination on the ecliptic, with the perihelion very close to the orbit of Venus, and with the aphelion close to the orbit of Mars. Moreover, we have derived

the Tisserand's parameter relative to Jupiter as 5.480 which would certainly indicate an asteroidal origin.

The parent asteroid of the Traspena meteorite is one of the six parent meteoroids and asteroids known so far that crossed both the orbits of Venus and Mars and, interestingly, did so with both the shortest semi-major axis and the lowest eccentricity of all of them as

Table 10. The heliocentric orbit of the Traspenna parent asteroid. Orbital elements are referred to the J2000 equinox. Tisserand’s parameter relative to Jupiter together with ratios between the orbital period of the parent asteroid and those of Jupiter, Mars, and Venus, respectively, are given in the last four rows.

Quantity	Value	
Geocentric radiant (RA) ($^{\circ}$)	α_R	126.52 ± 0.57
Geocentric radiant (Dec) ($^{\circ}$)	δ_R	30.77 ± 0.13
Geocentric velocity (km s^{-1})	v_g	12.11 ± 0.40
Radiant (constellation)	Cancer	
Orbital period (yr)	P	1.193 ± 0.025
Perihelion passage (JD)	T	$2\,459\,293.20 \pm 0.88$
		2021 March 19 at 16:48 UTC
Eccentricity	e	0.386 ± 0.013
Semimajor axis (au)	a	1.125 ± 0.016
Inclination ($^{\circ}$)	i	4.55 ± 0.19
Longitude of the asc. node ($^{\circ}$)	Ω	297.8270 ± 0.0003
Argument of the perihelion ($^{\circ}$)	ω	273.93 ± 0.98
Longitude of the perihelion ($^{\circ}$)	ϖ	211.76 ± 0.98
Perihelion distance (au)	q	0.6914 ± 0.0076
Aphelion distance (au)	Q	1.559 ± 0.035
True anomaly ($^{\circ}$)	f	266.08 ± 0.97
Tisserand’s parameter	T_{Jupiter}	5.480 ± 0.062
P_{Jupiter}/P		9.94 ± 0.20
P_{Mars}/P		1.576 ± 0.032
P_{Venus}/P		0.516 ± 0.011

shown in Fig. 20. In addition, it was as well the sixth parent meteoroid or asteroid with the shortest distance at the aphelion.

Unlike the identifications between meteor showers and comets, which were clearly established from the second half of the 19th century with the notable examples of the Perseids and Leonids (Schiaparelli 1867), the relationship between meteoroid streams and asteroids is much more recent. Meteoroids (which can eventually produce meteorites) are generated in collisions between asteroids with resulting velocities much smaller than the orbital velocity, so the orbits of young meteoroids are very similar to those of their parent bodies (Davis et al. 1979). In this way, Drummond (1982) searched plausible associations of NEAs with current meteoroid streams using the function D_D (Drummond 1981) to estimate distances between orbits. Later, Halliday, Blackwell & Griffin (1990) suggested the existence of streams of fragments that cross the Earth’s orbit and are responsible for a considerable fraction of the meteorites that fall to Earth. At present, dynamic associations between well-documented meteorites have been thoroughly studied (Spurný et al. 2003) and even impacts of asteroids have been predicted before falling as meteorites since the first case of the asteroid 2008 TC₃ (Jenniskens et al. 2009).

In order to determine membership in known meteoroid streams, Southworth & Hawkins (1963) were the first to introduce a distance function, $D_{SH}(e, a, i, \Omega, \omega)$, with which to measure the dissimilarity of two orbits. A widely used modification of that, $D_D(e, a, i, \Omega, \omega)$, was given by Drummond (1981) and Jopek (1993) proposed a hybrid function, $D_J(e, a, i, \Omega, \omega)$, alternative to the first two. Moreover, Steel, Asher & Clube (1991) and Asher, Clube & Steel (1993) proposed other functions, $D_{SAC}(e, a, i)$ and $D_{ACS}(e, a, i)$, respectively. The latter two may be useful to study very broad streams having a wide arc of nodal longitudes. Usually, certain previously established threshold values of these functions are considered to determine whether or not there is a dynamic association but we believe that this is not justified in

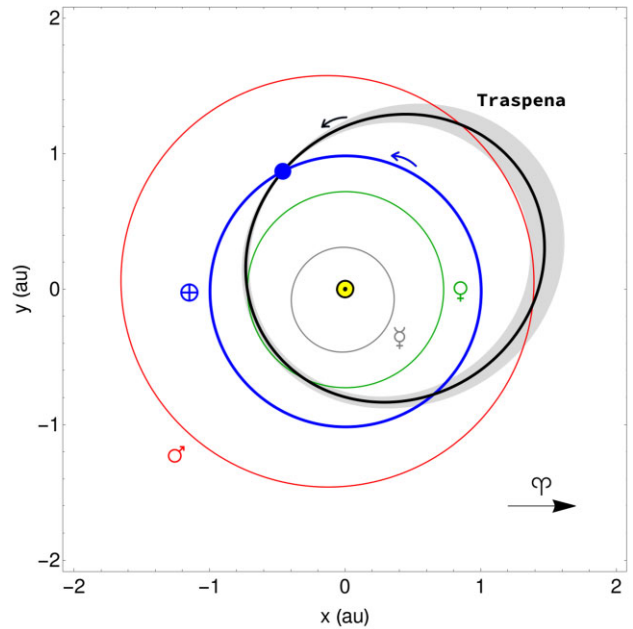


Figure 19. The heliocentric orbit for the parent asteroid of the Traspenna meteorite as seen from the ecliptic north pole is shown in black. The actual orbital inclination is $4^{\circ}55'$. The light grey region represents the likelihood computed from 10^4 Monte Carlo simulations based on the formal uncertainties of the radiant and the pre-atmospheric velocity. The orbits of Mercury, Venus, Earth, and Mars are shown in light grey, green, blue, and red, respectively, and the Earth’s position in its orbit is shown by a small blue disc. The small curved arrows indicate the motion of the Earth and that of the Traspenna parent asteroid while the arrow at the bottom right shows the direction to the point of the vernal equinox.

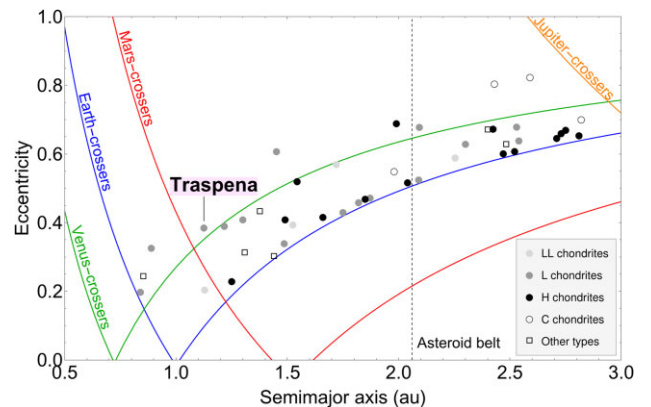


Figure 20. Distribution in the (a, e) diagram of the parent meteoroids and asteroids of the well-documented meteorites listed in Table 9. Traspenna is the Venus- and Mars-crosser with both the shortest semi-major axis and the lowest eccentricity.

the case of asteroids and that these functions only allow the selection of parent asteroid candidates. Furthermore, all these functions violate the triangle inequality and cannot, therefore, be formally defined as metrics but rather as quasimetrics as they satisfy a relaxed triangle inequality (Milanov, Milanova & Kholshchevnikov 2019).

Nevertheless, several actual metrics have been defined recently that allow the calculation of distances between Keplerian orbits in a rigorous way (Kholshchevnikov 2008). Thus, in our analysis, we have primarily considered the metric $\varrho_2(p, e, i, \Omega, \omega)$ given by

Table 11. Similarity between orbits of the asteroids with possible dynamic associations in the five-dimensional space \mathbb{H} of all Keplerian orbits (asteroids are ordered according to the value of the metric q_2 , so Minos would be the asteroid with the tenth lowest value), in the three-dimensional quotient space \mathbb{H}_5 , and in the four-dimensional spaces \mathbb{H}_3 and \mathbb{H}_4 of all Keplerian orbits (for the sake of brevity, only Minos values are shown in the quotient spaces). Absolute magnitudes are listed in the second column.

Asteroid	H_a	Five-dimensional space \mathbb{H}			
		q_2	D_{SH}	D_D	D_J
2022 AZ	23.91	0.0544	0.0752	0.0654	0.0678
2015 BF	26.60	0.0684	0.0853	0.0618	0.0753
2014 PG51	20.70	0.0738	0.0811	0.0837	0.0783
2017 PZ26	26.90	0.0798	0.0773	0.0981	0.0767
2019 AX14	26.68	0.0894	0.1055	0.0837	0.1006
2014 SD224	22.36	0.0972	0.0860	0.0835	0.0823
2019 AV	24.30	0.1010	0.1498	0.0977	0.1074
2018 BD	30.10	0.1030	0.1220	0.1532	0.1139
2015 PA57	24.50	0.1053	0.1224	0.0687	0.1108
1989 QF (Minos)	18.57	0.1059	0.1099	0.0487	0.1094
		Three-dimensional quotient space \mathbb{H}_5			
		q_5	D_{SAC}	D_{ACS}	
1989 QF (Minos)		0.0277	0.0326	0.0300	
		Four-dimensional quotient spaces			
		\mathbb{H}_3	\mathbb{H}_4		
		q_3	q_4		
1989 QF (Minos)		0.0508	0.0636		

Kholshevnikov et al. (2016)

$$q_2^2 = (1 + e_1^2)p_1 + (1 + e_2^2)p_2 - 2\sqrt{p_1 p_2}(\cos I + e_1 e_2 \cos P), \quad (26)$$

with

$$\begin{aligned} \cos I &= \cos i_1 \cos i_2 + \sin i_1 \sin i_2 \cos(\Omega_1 - \Omega_2), \\ \cos P &= \sin i_1 \sin i_2 \sin \omega_1 \sin \omega_2 + (\cos \omega_1 \cos \omega_2 \\ &\quad + \cos i_1 \cos i_2 \sin \omega_1 \sin \omega_2) \cos(\Omega_1 - \Omega_2) \\ &\quad + (\cos i_2 \cos \omega_1 \sin \omega_2 - \cos i_1 \sin \omega_1 \cos \omega_2) \\ &\quad \times \sin(\Omega_1 - \Omega_2), \end{aligned}$$

where p_1 and p_2 are the semilatus rectum of each orbit. This provides the actual distance between two Keplerian orbits ($\varepsilon_1, \varepsilon_2$) on the five-dimensional space \mathbb{H} of all Keplerian orbits. In addition, metrics $q_3(p, e, i, \omega)$, $q_4(p, e, i, \Omega)$, and $q_5(p, e, i)$ given in the same paper, provide the minimum distances between the orbits on three- and four-dimensional quotient spaces of all Keplerian orbits whose elements are the class of orbits with fixed p , e , and i values and all possible values of Ω and/or ω . This type of metrics may be of interest when orbital nodes and/or periastra undergo secular perturbations whereas the remaining elements change slowly.

We have accomplished a search for a possible asteroidal parent body of the Traspenna meteorite among the NEOs taking their orbital elements from the Small-Body DataBase (SBDB) of the JPL Solar System Dynamics & Center for NEO Studies (CNEOS) and measuring the similarity between orbits by means of the mentioned q -metrics. Anyhow, values of the most used D -functions were also calculated and compared with the former. Results derived from q -metrics and D -functions for the most probable dynamic associations of a total of 29 430 NEOs (SBDB accessed on 2022 July 11) are shown in Table 11.

Table 12. q -metrics and D -functions ordered according to the p -values obtained with the Monte Carlo procedure used to assess the probability of attaining these small orbital distances as regards the hypothetical Traspenna–Minos dynamic association.

q -metrics and D -functions	Draws	p -value
q_2	53 743 \pm 539	0.0319
D_D	19 395 \pm 194	0.0884
D_{SH}	14 472 \pm 143	0.1185
D_J	8546 \pm 85	0.2007
q_3	30 818 \pm 315	0.0556
q_4	12 300 \pm 123	0.1394
q_5	7344 \pm 72	0.2335
D_{SAC}	1983 \pm 19	0.8649
D_{ACS}	1731 \pm 17	0.9908

The most prominent asteroid with which Traspenna could be associated is Minos, also known as 6239 Minos and 1989 QF (Shoemaker et al. 1989). This is a bright ($H_a = 18.57$ mag) NEA, classified as a potentially hazardous asteroid (PHA) of the Apollo group, with a size of about 0.5 km and a rotation period of 3.6 h. To assess the probability of attaining this small orbital distance, we have followed a Monte Carlo procedure considering not only the distance between orbits but the absolute magnitude as well (Borovička et al. 2013b). We have used a debiased orbit and absolute–magnitude distribution model containing 802 000 synthetic NEOs (with $17 < H_a < 25$) parametrized by their orbits and absolute magnitudes (Granvik et al. 2018).

Therefore, to calculate the expected probability of such small distance, we have carried out a null hypothesis significance testing considering the null hypothesis H_0 : *the asteroid Minos and Traspenna are not dynamically associated*, where we understand that two bodies are dynamically associated if they reside in nearly identical heliocentric orbits with this common motion suggesting a joint formation scenario caused by asteroid collisions or by the rotational fission of a rubble pile. Thus, we have extracted random pairs of synthetic NEOs from the database until one case with a shorter distance than that between Traspenna and Minos was obtained. We repeated this procedure 10^4 times, recording the number of draws needed each time to find a match. We obtained an average of $53\,743 \pm 539$ draws using the metric q_2 . Considering that there are 1715 NEOs of the size of Minos or larger, this gives a p -value of 0.0319. All p -values obtained for the whole set of q -metrics and D -functions are listed in Table 12 and, in addition, a bar chart plot is shown in Fig. 21.

The only metric with a p -value below the typical threshold of 0.05 for the significance level is q_2 . Of the remaining metrics, the best performing is q_3 , that is defined in the metric space \mathbb{H}_3 in which e , a , i , and ω are fixed and Ω takes all possible values. This could be interpreted as that the hypothetical dynamic association may not depend on the node angles. In this case, the dynamical link would persist even if there were a long-term precession of the orbits. With respect to the D -functions, none of them allow in any way to reject the null hypothesis, so that if, as usual, we were to use these functions as criteria to determine a possible association between Traspenna and Minos, we should definitely rule out such a possibility.

Nevertheless, based on the p -value obtained for the primary metric q_2 , we reject the null hypothesis, H_0 , at a significance level of 0.05 (corresponding approximately to 2σ), in favour of the alternative hypothesis. In this way, we can say that there is some evidence at this level to conclude that Traspenna and Minos are dynamically

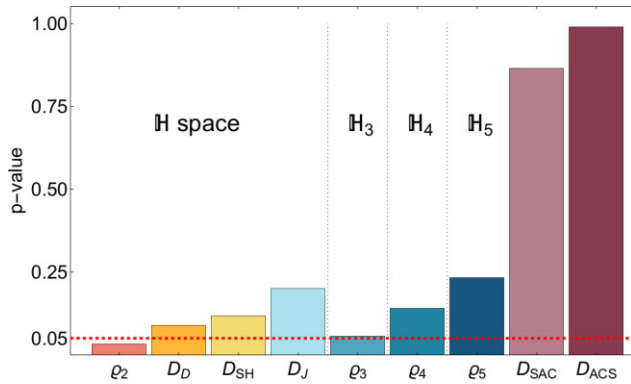


Figure 21. Bar chart plot showing p -values obtained for the hypothetical Traspena–Minos dynamic association considering the whole set of ρ -metrics and D -functions ordered according to the metric space in which they are defined. The red dashed line indicates the typical threshold of 0.05 for the significance level.

associated, possibly the former being a fragment produced during a mass-shedding event in the past. However, this evidence is weak and we would prefer to have at least a 3σ -level association as customary in physics, in order to be convinced more conclusively of the evidence for such an association.

Therefore, we cannot conclusively state that there is a dynamic link between Traspena and the asteroid Minos. As a matter of fact, we must take into account that the orbits of meteorites originating from asteroids have probably been chaotically modified under the influence of the Yarkovsky effect, orbital resonances, and close encounters with the inner planets during millions of years (Vokrouhlický & Farinella 2000). Hence, we acknowledge that more studies are needed assessing the likelihood of past orbital convergence of the Traspena orbit and that of Minos. In this way, a long-term backward integration could be interesting in order to investigate their dynamics as well as hypothetical resonances with the inner planets. Regarding the latter, we should consider that resonances with Venus, Earth, and Mars in the region $1 < a < 2.5$ au would be at least as strong as resonances with Jupiter (Gallardo 2006).

6 ANALYSIS OF THE METEORITE

6.1 Methodology

The bulk meteorite was first examined by X-ray computed tomography (micro-CT) with a Nikon- XTH 160 system equipped with a Varex 2520DX flat-panel detector at the *Museo Nacional de Ciencias Naturales* (MNCN-CSIC). The bulk density of the meteorite was measured with a hydrostatic Westphal balance using distilled water at 4°C . Then, the meteorite was sliced into two parallel cuttings in order to obtain several fresh fragments and thin sections to characterize the meteorite with different physical and chemical methods.

Scanning electron microscopy (SEM) images and mineral chemistry analyses were carried out by Electron probe microanalysis (EPMA) on a JEOL JXA-8230 instrument equipped with five wavelength-dispersive spectrometers (WDS) at the Scientific and Technological Centres of the University of Barcelona (CCiTUB). Spot analyses had an accelerating voltage of 20 kV, a beam current of 15 nA, and a spot size of 1–2 micrometers. Analytical standards used were: hematite (Fe, LIF, $K\alpha$), rutile (Ti, PET, $K\alpha$), periclase (Mg, TAP, $K\alpha$), rhodonite (Mn, LIF, $K\alpha$), Al_2O_3 (Al, TAP, $K\alpha$), Cr_2O_3 (Cr, PET, $K\alpha$), NiO (Ni, LIF, $K\alpha$), metallic cobalt (Co, LIF,

$K\alpha$), diopside (Si, TAP, $K\alpha$), fluorapatite (P, PET, $K\alpha$), pyrite (S, PET, $K\alpha$), wollastonite (Ca, PET, $K\alpha$), orthoclase (K, PET, $K\alpha$), and albite (Na, TAP, $K\alpha$).

Magnetic susceptibility measurements were performed on five meteorite fragments (28×48 mm) using an Agico KLY4 instrument as well as a Bartington MS3-Magnetic Susceptibility System, and recording 10 measurements for each fragment, by the *Instituto Geográfico Nacional* (IGN). Magnetic hysteresis and remanence curves were analysed with a Coercivity Spectrometer developed by Kazan University (maximum applied field of 500 mT, nine measurements per point, increments of 0.5 mT). The Natural Remanent Magnetization (NRM) of the meteorite fragments was measured with an Agico JR5A spinner magnetometer, shielded from external field by self-compensated Helmholtz coils.

About 1 g of the meteorite was carefully grinded and homogenized to obtain a powder for X-ray diffraction (XRD) analyses which were performed on a Bruker D8-A25 instrument equipped with a Cu X-ray source (Cu $K\alpha$ radiation) and a LynxEye position sensitive detector at *Geosciences Barcelona*. The XRD scans were acquired between 4° and 70° in 2θ with a 0.016° step size and equivalent counting times of 346 s. Phase identification was carried out by using the DIFFRAC.EVA software together with the Powder Diffraction File (PDF-2) data base. The Rietveld method (Young 1993) was employed in order to obtain information about mineral abundances in the meteorite and also about the Fe/Mg content of the major silicate phases. For the Rietveld analyses, the TOPAS 4.2 software from Bruker was used. Preferential orientation effects were considered for some of the phases by using the March–Dollase algorithm (Young 1993).

6.2 Description, composition, and petrography

The Traspena meteorite weighed 527.0 g and was totally covered by a black and well-developed fusion crust showing several thumb-sized regmaglypts (Fig. 18). The bulk density is 3.25 ± 0.01 g cm $^{-3}$ and the magnetic susceptibility is $\log \chi (\times 10^{-9} \text{ m}^3 \text{ kg}^{-1}) = 4.89$. These values compare well with the values reported for L-type ordinary chondrites (Rochette et al. 2003; Consolmagno et al. 2006). Fig. 22 shows micro-CT images of the bulk meteorite corresponding to the 3D distributions of mineral sizes and grains with higher densities (FeNi metal and FeS), respectively. X-ray tomography results indicate that metal grains are grouped in certain areas but there is no agglomeration of metal phases in shock veins or cracks. In addition, no porosity was observed.

The petrographic and mineralogical study of the meteorite carried out by optical microscopy of transmitted light and SEM (BSE) reveals the occurrence of chondrules set in a recrystallized silicate matrix, with an apparent diameter ranging from ca. 0.4 to 2 mm. These chondrules exhibit porphyritic olivine pyroxene (POP), barred olivine (BO), and granular olivine pyroxene (GOP) textures (Figs 23 and 24). FeNi-metal, troilite (Tro), and chromite (Chr) are observed throughout. Most plagioclase (Pl) grains exhibit sizes of 5–50 μm . FeNi metal grains are often surrounded by brown metal oxides (Fig. 23b). Micro-XRD measurements indicate that they correspond to trevorite-type ferroan phases, $(\text{Ni,Fe})\text{Fe}_2\text{O}_4$, which is also in accordance with a mineral phase showing high coercivity. Olivine (Ol) grains contain planar fractures and exhibit undulatory extinction, indicating shock stage S3 (Stöffler, Keil & Scott 1991).

Powder XRD measurements allowed us to perform a semiquantitative bulk analysis of the major minerals in the meteorite. The XRD pattern is dominated by reflections from Ol (forsterite) and low-Ca pyroxene (orthoenstatite). In addition, weaker features arising from Pl feldspar, Tro, and Kam can be identified. Semiquantitative

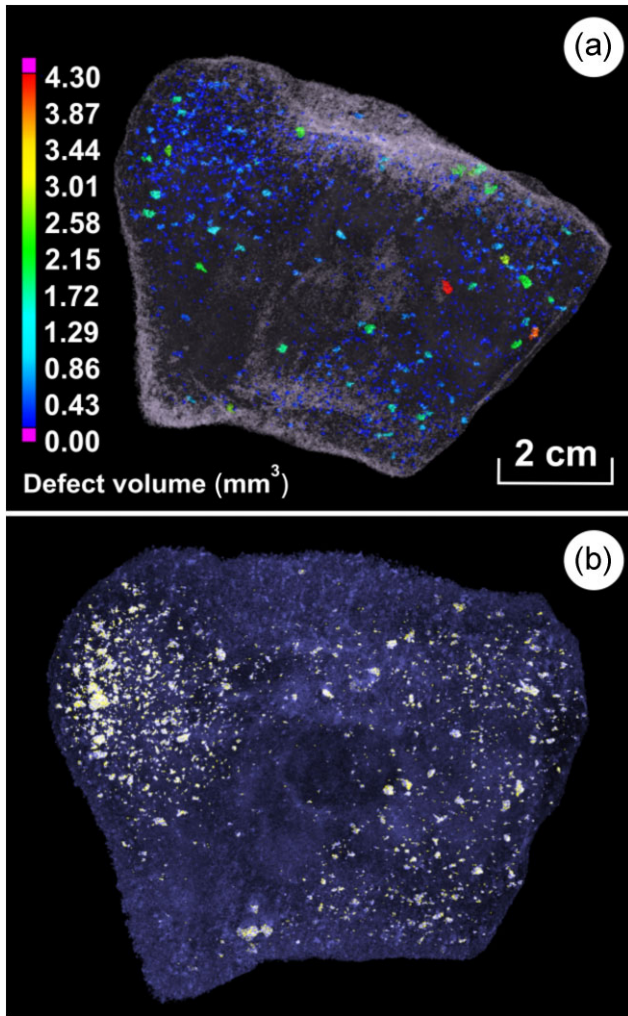


Figure 22. Micro-CT-Scan Images of the Traspenna meteorite: (a) 3D projections of mineral sizes and (b) distribution of mineral grains with higher densities.

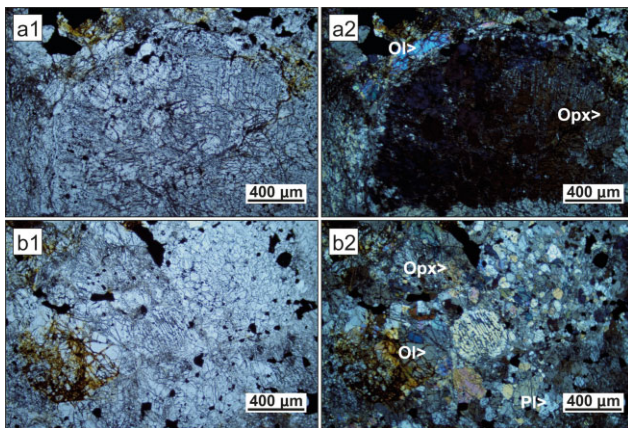


Figure 23. Optical microscope images obtained with transmitted light (1) and cross-polarized light (2). Figures a1 and a2 show an elongated olivine-rich (Ol) chondrule with interstitial orthopyroxene (Opx). Figures b1 and b2 show a barred chondrule comprised of alternating Ol and Opx surrounded by subhedral grains of the typical mineral association: Ol, Opx, Pl, and accessory sulfides, FeNi metal, and oxides.

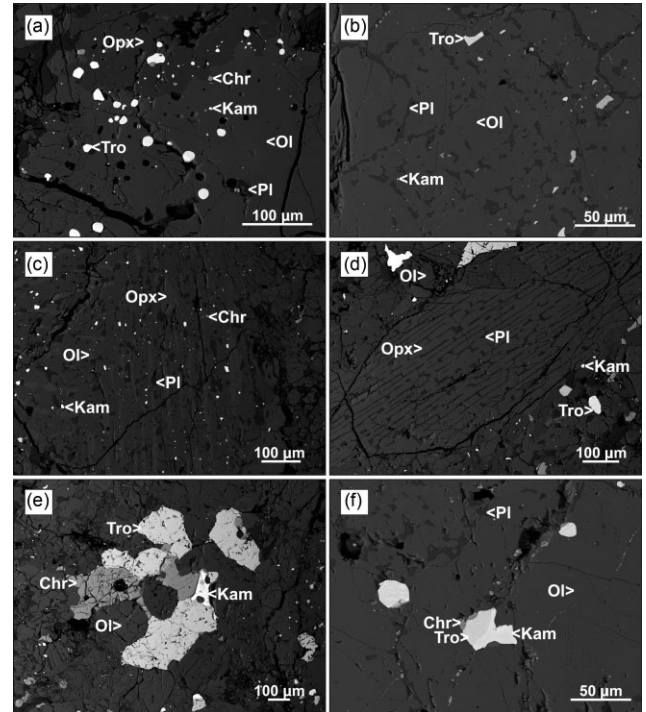


Figure 24. SEM (BSE) images: (a) Subhedral to anhedral Tro and kamacite (Kam) grains associated with a silicate matrix formed by Ol, Opx, and Pl with accessory Chr; (b) Ol-rich chondrule with interstitial Pl and accessory subhedral grains of Tro, and Kam; (c) Typical elongated barred texture comprised of alternating bands of Ol and combined Opx, and Pl; (d) Euhedral Opx crystal with alternating bands of Pl, surrounded by Ol and accessory Tro, and Kam; (e), (f) Subhedral to anhedral Tro and Kam grains associated with Chr in a typical Ol granular matrix with interstitial Pl.

Table 13. Lattice parameters and cationic compositions for the main silicate minerals (forsterite and orthoenstatite) as obtained from Rietveld analysis of powder XRD.

	Forsterite	Orthoenstatite
a (Å)	4.774 (1)	18.286 (1)
b (Å)	10.271 (1)	8.866 (1)
c (Å)	6.013 (1)	5.205 (1)
Mg (mol per cent)	74	75
Fe (mol per cent)	26	20
Ca (mol per cent)	–	5

mineralogical composition as obtained from Rietveld analysis yields ca. 44 per cent Ol, 43 per cent low-Ca pyroxene, 8 per cent Pl feldspar, 4 per cent Tro, and 1 per cent FeNi metal. The modal abundances found for Ol and low-Ca pyroxene are close to those typically found in ordinary chondrites (Dunn et al. 2010a, b). Unit-cell refinement of forsterite and enstatite, in combination with the data of Morrison et al. (2018) regarding the compositional dependence of unit-cell parameters of minerals in rocks and extraterrestrial bodies, has also allowed us to evaluate the average cationic composition of the two major minerals in the meteorite. Table 13 shows the refined lattice parameters of forsterite and orthoenstatite, together with their corresponding average Mg/Fe and Mg/Fe/Ca contents, which correspond to Fa = 26 per cent in Ol and Fs = 20 per cent in low-Ca pyroxene. These values suggest that Traspenna is a L-type chondrite. The fact that no monoclinic pyroxene phase is detected by XRD, and the observation of well-defined reflections for the Ol and

Table 14. Mean compositions (wt. per cent) of the Traspenna meteorite metal and sulfide phases as obtained by EPMA.

	Kamacite	Taenite	Troilite
Number of grains	10	11	24
Si	<0.1	<0.1	<0.1
Mn	<0.1	–	<0.1
Fe	86.0 ± 8.7	67.2 ± 3.3	64.1 ± 0.4
Co	0.8 ± 0.2	0.4 ± 0.2	<0.1
Ni	13.2 ± 9.2	32.6 ± 3.0	–
P	–	–	–
S	–	–	36.0 ± 0.4
Total	100.1 ± 0.8	100.2 ± 0.8	100.2 ± 0.4

Table 15. Mean compositions (wt. per cent) of the Traspenna meteorite silicates and chromite as obtained by EPMA.

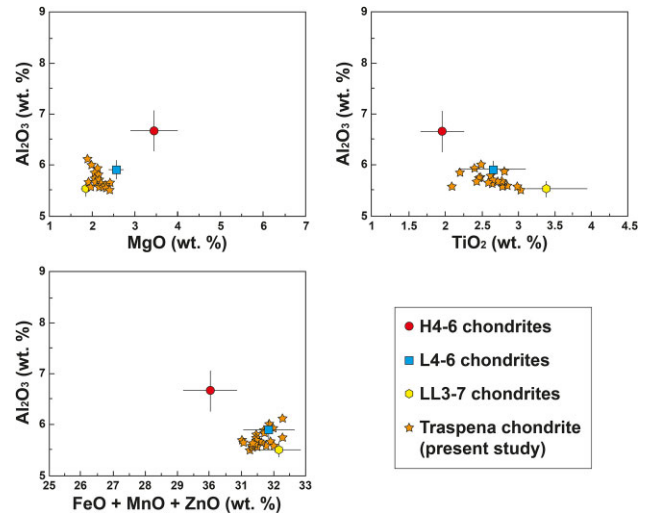
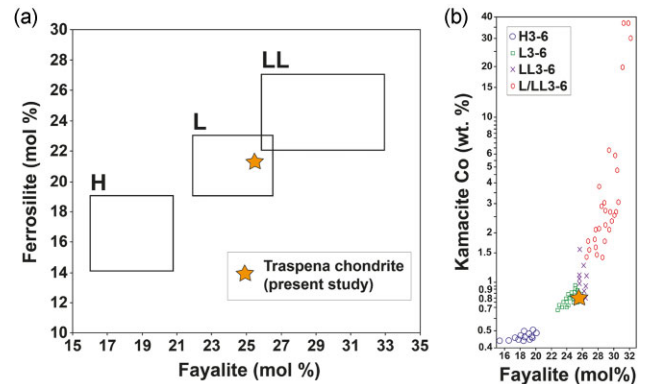
	Olivine	Low-Ca Pyroxene	Plagioclase	Chromite
Number of grains	10	11	24	21
SiO ₂	38.0 ± 0.6	51.1 ± 0.7	65.1 ± 0.8	<0.1
TiO ₂	<0.1	0.2 ± 0.1	–	2.6 ± 0.1
Al ₂ O ₃	–	<0.1	21.2 ± 0.3	5.7 ± 0.4
Cr ₂ O ₃	<0.1	<0.1	–	55.8 ± 1.1
FeO	23.2 ± 0.8	14.1 ± 0.4	0.5 ± 0.2	30.8 ± 0.6
MnO	0.5 ± 0.1	0.5 ± 0.1	<0.1	0.8 ± 0.1
MgO	38.1 ± 0.7	28.7 ± 0.5	<0.1	2.3 ± 0.4
CaO	–	0.8 ± 0.3	2.2 ± 0.2	<0.1
Na ₂ O	<0.1	<0.1	9.6 ± 0.9	–
K ₂ O	–	<0.1	1.0 ± 1.0	–
NiO	<0.1	<0.1	–	<0.1
CoO	–	–	–	<0.1
Total	99.8 ± 0.6	99.7 ± 0.8	99.5 ± 1.0	98.2 ± 1.0
End member	Fa _{25.5} ± 0.6	Fs _{21.3} ± 0.5 Wo _{1.5} ± 0.7	Ab _{84.1} ± 3.2 Or _{5.4} ± 2.0	

pyroxene phases implying high compositional homogeneity, indicate high petrological grade.

6.3 Mineral chemistry and classification

Table 14 shows the mean compositions of metal and sulfide phases as obtained by electron microprobe analysis (EPMA). The composition of Kam is 86.0 ± 8.7 wt. per cent Fe, 13.2 ± 9.2 wt. per cent Ni, and 0.8 ± 0.2 wt. per cent Co, and that of taenite is 67.2 ± 3.3 wt. per cent Fe, 32.6 ± 3.3 wt. per cent Ni, and 0.4 ± 0.2 wt. per cent Co. The composition of Tro is very homogeneous, 64.1 ± 0.4 wt. per cent Fe and 36.0 ± 0.4 wt. per cent S. Table 15 shows the mean compositions of silicate phases and chromite obtained by EPMA. The Ol composition is Fa 25.5 ± 0.6 mol percent (range of 24.5–26.1 mol percent), the low-Ca pyroxene composition is Fs 21.3 ± 0.5 mol percent (range of 20.9–21.8 mol percent), Wo 1.5 ± 0.7 mol percent (range of 0.97–2.0 mol percent), and the Pl composition is Ab 83.9 ± 3.8 mol percent (range of 80.1–85.4 mol percent), Or 5.4 ± 2.7 mol percent (range of 8.1–4.3 mol percent). The good agreement between the data obtained for the major silicate phases, Ol and pyroxene, by EPMA (see Table 15) and XRD (see Table 13), should be remarked.

Fig. 25 shows the chromite composition of the Traspenna meteorite along with mean values for H, L, and LL ordinary chondrites (Bunch,


Figure 25. Plot of the chromite composition of the Traspenna meteorite along with mean values for H, L, and LL ordinary chondrites (Boschi et al. 2017).

Figure 26. Plot of (a) the mean Ol and pyroxene compositions and (b) the Co content in Kam of the Traspenna meteorite along with mean values for H, L, and LL ordinary chondrites (Rubin 1990; Grossman & Rubin 2006).

Keil & Snetsinger 1967; Wlotzka 2005; Boschi et al. 2017). Fig. 26 shows the mean Ol and pyroxene compositions (a) and Co content in Kam (b) of the Traspenna meteorite along with mean values for H, L, and LL ordinary chondrites (Rubin 1990; Grossman & Rubin 2006). Based on the mineral composition values, absence of monoclinic pyroxene, presence of chondrules, size of Pl grains, modal distribution, bulk density, and magnetic susceptibility values, the Traspenna meteorite is classified as a L5 ordinary chondrite.

7 CONCLUSIONS

The approximate cumulative frequency of impacts from objects larger than D metres across was estimated by Brown et al. (2002b) to be $N = 10^{c_0} D^{-d_0}$, being $c_0 = 1.568 \pm 0.030$ and $d_0 = 2.70 \pm 0.08$. Thus, about 25 objects like the Traspenna asteroid collide with the Earth every year which means that, in a region the size of Galiza, we would have to wait nearly 700 yr to see such a meteorite fall (and about 35 yr for a similar event to take place in the whole of the Iberian Peninsula). This would explain why Traspenna is the first well-documented meteorite to fall in Galiza and to be recovered.

This fall took place on 2021 January 18 at 00:18:56.54 UTC and although clouds and fog considerably affected some of the

observations, it was possible to calculate an accurate atmospheric trajectory, as well as the expected strewn field, and even a very precise pre-entry heliocentric orbit.

The original asteroid, with a mass of 2620 kg and a diameter of 1.15 m, had a pre-atmospheric velocity of 16.42 km s^{-1} . It entered the atmosphere at 75.10 km of height and finished its luminous flight at 15.75 km of height with a velocity of 2.38 km s^{-1} . The slope of the atmospheric trajectory was $76^\circ 7051$ and the kinetic energy was estimated to be 0.0844 kt TNT.

We have detected the coupling at the seismic stations of the direct sound wave with an average sound propagation speed of $278 \pm 93 \text{ m s}^{-1}$ which is compatible with the direct sound wave at the seismic station. On the other hand, seismic waves corresponding to the emission of sound waves by the hypersonic flight (cylindrical, surface waves) and sound waves corresponding to ablations (spherical waves) were identified, and their frequency content was found to peak at around 15 Hz. The three component (NS, EW, Z) characteristics of the event signals at the three stations show a clear NS directivity at the ECAL station and a similarity of morphology for the EPON and EAGO stations which are transverse to the trajectory. Finally, each of the main ablations were calibrated as a source emitting energy between 2×10^7 and 1.3×10^{10} J.

The mass-loss of the meteoroid through the Earth's atmosphere was derived using a new four-parameter mathematical model (based on the hyperbolic tangent function) which provides an explicitly time-dependent expression. The physical parameters needed to fit the model were obtained from a non-linear least-squares minimization using the differential evolution method. This model not only fitted the experimental data very well, but also provided the time interval at which the meteoroid experienced the maximum ablation regime as well as the time at which the mass-loss was maximum together with its value, i.e. $1.81 \times 10^3 \text{ kg s}^{-1}$ at 2.75 s from the beginning of the bolide. Consequently, the meteoroid would have lost the half of its mass in less than a second.

The first large fragmentation occurred at a height of 35 km under an aerodynamic pressure of 1.52 MPa and the sole recovered meteorite survived intact at maximum pressure of 7.84 MPa. This weighed 527 g and was recovered 2 month after the fall at a distance of 31 m from the nominal position of the impact point calculated after the dark flight. We estimate that some meteorites may still be out there, in particular, two fragments of masses around 0.25 and 0.14 kg distributed as shown in Fig. 16.

The Traspesa meteorite is a L5 S3 ordinary chondrite. It has a bulk density of $3.25 \pm 0.01 \text{ g cm}^{-3}$ and a magnetic susceptibility of $\log \chi (\times 10^{-9} \text{ m}^3 \text{ kg}^{-1}) = 4.89$. It contains POP, BO, and GOP chondrules with an apparent diameter of 0.4–2 mm. The Ol composition is Fa 25.5 ± 0.6 mol per cent and the low-Ca pyroxene composition is Fs 21.3 ± 0.5 mol per cent and Wo 1.5 ± 0.7 mol per cent. There is no monoclinic pyroxene. The size of the Pl grains is 5–50 μm and their composition is Ab 83.9 ± 3.8 mol per cent and Or 5.4 ± 2.7 mol per cent. Kam contains 13.2 ± 9.2 wt. per cent Ni and 0.8 ± 0.2 wt. per cent Co.

The parent asteroid was an Apollo-type object orbiting the Sun with an orbital period of 1.193 yr on a moderately eccentric orbit, 0.386, with a low inclination, $4^\circ 55'$. Its perihelion was inside the Venus orbit and the aphelion just beyond the orbit of Mars. With a Tisserand's parameter of 5.480, this is an orbit with a clear asteroidal origin. It is worth mentioning that the parent asteroid of the Traspesa meteorite is the Venus- and Mars-crosser with both the shortest semi-major axis and the lowest eccentricity. On the other hand, research on the hypothetical dynamic link of Traspesa with the PHA Minos is inconclusive because even though new metrics in the space of

all Keplerian orbits provide some evidence in its favour, this shows weak statistical significance and therefore further studies are needed.

During this research, new mathematical models and an original software were developed at the *Escola Politécnica Superior de Enxeñaría* (EPSE-USC) to determine both the atmospheric trajectory of the meteoroid through the Earth's atmosphere and the dark flight, taking into account as many variables as possible. In addition, the application of these techniques to a few individual fragments for which astrometric measurements were available allowed to obtain a strewn field with the most probable fall locations for each of them. In parallel, the development of new computing tools was necessary to carry out these tasks. Therefore, procedures based on optimization algorithms and on Monte Carlo techniques were routinely incorporated into the new software in order to automate the complete calculation workflow from the astrometric measurements of the Traspesa superbolide position to the determination of the heliocentric orbit and the search for potential dynamic associations with NEOs.

However, we would like to point out that no deterministic model, no matter how sophisticated, can account for absolutely all parameters due to lack of knowledge about them, e.g. the initial shape of the meteoroid, its strength, the actual winds during the dark flight, and so on. In our opinion, the most decisive factors, usually unknown, are the actual details of the fragmentations during the atmospheric trajectory and, above all, the actual winds acting in the dark flight. Regarding the former, we must accept, as Spurný et al. (2020) have already observed, that any fragmentation model is not able to reveal all details of the fragmentation process and that actually this is probably more complicated. On the other hand, concerning the influence of the wind field on the determination of dark flight, Ceplecha (1987) pointed out that poor knowledge was one of the main complications in the computations. We agree, as recent studies using Monte Carlo simulations have shown, that the main factor contributing to the shape, size, and location of the strewn field is the atmospheric wind profile (Moilanen, Gritsevich & Lyytinen 2021). Thus, drifts in the computed position of each fragment would be expected as well in the case of Traspesa. These could be up to 300 metres according to estimates by Andreić (2012). Nevertheless, in this case, we have practically found the exact impact location of the main body, as the difference between the calculated and the actual locations where the meteorite was found is only of 31 m. This would be indeed the best proof of the validity of the mathematical models and methods developed and the assumptions adopted.

ACKNOWLEDGEMENTS

The authors would like to start by expressing their deepest gratitude to their colleagues from the Department of Applied Mathematics in the *Campus Terra* of Lugo (USC) for their perseverance and tireless work in the search for possible meteorites (in alphabetical order of surnames): Gerardo Casal, Juan B. Ferreiro, Duarte Santamarina, Miguel E. Vázquez-Méndez, and Miguel A. Vilar. The same grateful acknowledgement goes to the other members of the search team who occasionally participated in the searches: Chelo Astorgano, Ana Cabana, Pedro Ferreiro, Marolas Leis, Cidre Santamarina, Sarela Santamarina, and Paula Vázquez.

We are also grateful to Jesús Á. Farelo (Lebruxo, Baralla) for his description of the meteorite recovery and to Marcos A. González for his efforts as director of the *Museo de Historia Natural* (MHN-USC) to ensure that this outstanding piece of the Galizian geological heritage became part of the collection of our most important museum and that it did not end up on the black market for meteorites.

We are indebted to those who shared their private videos and kindly let us into their homes or workplaces for on-site calibrations: Iris Fernández (from *Bodegas Descendientes de J. Palacios*, Corullón), Caroline Bureau and Fernando Rey (Nigrán), Sergio Eiras (Caldas de Reis), and Miguel Salguero and Francisco García (León) for providing us with their respective recordings of the bolide and for trying on different nights to obtain images of the starry background that allowed the astrometric calibration of the videos. Also to Sonia Cora (Ponferrada), Alejandro Marcos (Foncebadón), Alberto Campo (*Cementos Cosmos*, Toral de los Vados/Toural dos Vaos), and Eva Alonso (Pradanos del Tozo, Burgos).

We would like to thank Jaime Izquierdo and Antonio J. Robles for providing us with their video recordings from their stations applied to fireball monitoring in Madrid and Estepa (Seville), respectively.

We also thank Manuel Cortón (Lugo) for his willingness to describe to us the physical characteristics of the fireball as he saw it from his home; Gloria Millares (Pumarega, Castroverde); Vanessa Balboa and her parents, Luis Balboa and Esther Amado (Bande, Lánacara) for their interest in understanding what their cameras had captured; Julio Fernández and Nuria Rivas (Lánacara, Lánacara) for their concern to retrieve some recordings of the bolide; Carlos Vila (Piño, Pobra de Brollón) for his testimony about the time elapsed between the main glare and the arrival of the sound; and many anonymous people of regions of Lugo, Ancares, Sarria, Terra de Lemos, Quiroga, and Bierzo for their testimonials describing their experiences of the event.

We wish to acknowledge the support of Xuasús González (*Asociación Leonesa de Astronomía*) in some measurements carried out in the province of León as well as the work of Santiago Alfageme, surveyor of *Gesminle*. We are grateful as well to the *Aeródromo das Rozas* (Castro de Rei, Lugo), to the *Comandancia da Garda Civil* (Lugo), and to the newspaper *El Progreso* (Lugo) for publishing, at our request, a press release asking for the collaboration of people who might have a video of the bolide.

We would like to thank Soledad Álvarez Pousa (*Geosciences Barcelona*) for technical support with the XRD measurements. We also thank Marisa Osete and Vicente Carlos Ruiz for allowing us to use the instrumentation at the Paleomagnetism Laboratory of the Complutense University of Madrid. Supporting meteorological data were provided by Alberto Pettazzi (Departamento de Climatología e Observación, *MeteoGalicia*) and by Francisco Infante and Rafael Sánchez (*Agencia Estatal de Meteorología*, AEMET). Seismic data were provided by the *Instituto Geográfico Nacional* (IGN). Data on the asteroid orbits were downloaded from the JPL's Small Bodies Database (<https://ssd.jpl.nasa.gov>).

The authors are very grateful to Jérémie Vaubaillon for his helpful revision and comments on the manuscript.

This paper was supported by the *Xunta de Galicia* (Spain) under the ED431B 2020/38 grant.

We strongly encourage and thank in advance anyone who can recover a new fragment of this meteorite in the future to contact the first author in order to provide us with the most relevant information on its characteristics and to check the accuracy of the estimated fall locations.

Author contribution statement: Manuel Andrade: astrometry, photometry, acoustic analysis, atmospheric trajectory, mass-loss and fragmentation models, dark flight, strewn field, heliocentric orbit, dynamic associations with NEOs, meteorite searches, manuscript preparation, and supervision. José Á. Docobo: field measurements, astrometry, meteorite searches, and funding acquisition. Javier García-Guinea: petrography and geochemistry. Pedro P. Campo: field measurements, astrometry, and meteorite searches. Mar Tapia:

seismic analysis. Luis Sánchez-Muñoz: petrography and geochemistry. Víctor Villasante-Marcos: magnetic measurements. Eloy Peña-Asensio: astrometry. Josep M. Trigo-Rodríguez: astrometry and petrography. Jordi Ibáñez-Insa: X-ray diffraction. Marc Campeny: petrography and geochemistry. Jordi Llorca: petrography, geochemistry, and classification.

DATA AVAILABILITY

The data underlying this article will be shared on reasonable request to the corresponding author.

REFERENCES

- Andreev G., 1991, in Heinlein D., Koschny D., eds, Proc. Int. Meteor. Conf., 1990, The Influence of the Meteor Position on the Zenith Attraction. 9th IMC, Violau, Germany, p. 25
- Andreić Z., 2012, in Gyssens M., Roggemans P., eds, Proc. Int. Meteor. Conf., 2011, Dark Flight Calculations: How Accurate Can They Be?. 30th IMC, Sibiu, Romania, p. 23
- Artem'eva N. A., Shuvalov V. V., 1996, *Shock Waves*, 5, 359
- Asher D. J., Clube S. V. M., Steel D. I., 1993, *MNRAS*, 264, 93
- Barri N., 2010, *Arch. Comput. Method. Eng.*, 17, 1
- Barri N. G., Stulov V. P., 2003, *Solar Syst. Res.*, 37, 302
- Beech M., Brown P., 2000, *Planet. Space Sci.*, 48, 925
- Borovička J., 1990, *Bull. Astron. Inst. Czech.*, 41, 391
- Borovička J., Spurný P., Kalenda P., Tagliaferri E., 2003, *Meteorit. Planet. Sci.*, 38, 975
- Borovička J. et al., 2013a, *Meteorit. Planet. Sci.*, 48, 1757
- Borovička J., Spurný P., Brown P., Wiegert P., Kalenda P., Clark D., Shrbený L., 2013b, *Nature*, 503, 235
- Borovička J. et al., 2015, *Meteorit. Planet. Sci.*, 50, 1244
- Borovička J., Popova O., Spurný P., 2019, *Meteorit. Planet. Sci.*, 54, 1024
- Borovička J., Bettonvil F., Baumgarten G., Strunk J., Hankey M., Spurný P., Heinlein D., 2021, *Meteorit. Planet. Sci.*, 56, 425
- Boschi S. et al., 2017, *Geochim. Cosmochim. Acta*, 204, 205
- Bouquet A., Baratoux D., Vaubaillon J., Gritsevich M. I., Mimoun D., Mousis O., Bouley S., 2014, *Planet. Space Sci.*, 103, 238
- Brent R. P., 1973, *Algorithms for Minimization without Derivatives*. Englewood Cliffs, Prentice-Hall, NJ
- Bronshten V. A., 1983, *Physics of Meteoric Phenomena*. D. Reidel Publishing Company, Dordrecht
- Brown P., Ceplecha Z., Hawkes R. L., Wetherill G., Beech M., Mossman K., 1994, *Nature*, 367, 624
- Brown P. G., Revelle D. O., Tagliaferri E., Hildebrand A. R., 2002a, *Meteorit. Planet. Sci.*, 37, 661
- Brown P., Spalding R. E., ReVelle D. O., Tagliaferri E., Worden S. P., 2002b, *Nature*, 420, 294
- Brown P., Pack D., Edwards W. N., Revelle D. O., Yoo B. B., Spalding R. E., Tagliaferri E., 2004, *Meteorit. Planet. Sci.*, 39, 1781
- Brown P. et al., 2011, *Meteorit. Planet. Sci.*, 46, 339
- Brown P. G. et al., 2019, *Meteorit. Planet. Sci.*, 54, 2027
- Brykina I. G., Egorova L. A., 2021, *Adv. Astron.*, 2021, 1
- Bunch T. E., Keil K., Snetsinger K. G., 1967, *Geochim. Cosmochim. Acta*, 31, 1569
- Carter R. T., Jandir P. S., Kress M. E., 2009, *Lunar Planet. Sci. Conf. Estimating the Drag Coefficients of Meteorites for All Mach Number Regimes*Show affiliations. The Woodlands, Texas, 2059
- Ceplecha Z., 1961, *Bull. Astron. Inst. Czech.*, 12, 21
- Ceplecha Z., 1987, *Bull. Astron. Inst. Czech.*, 38, 222
- Consolmagno G. J., Macke R. J., Rochette P., Britt D. T., Gattacceca J., 2006, *Meteorit. Planet. Sci.*, 41, 331
- Davis D. R., Chapman C. R., Greenberg R., Weidenschilling S. J., Harris A. W., 1979, in Gehrels T., Matthews M. S., eds, *Asteroids*. The University of Arizona Press, Tucson, AZ, p. 528
- Devillepoix H. A. R. et al., 2018, *Meteorit. Planet. Sci.*, 53, 2212

- Devillepoix H. A. R. et al., 2022, *Meteorit. Planet. Sci.*, 57, 1328
- Docobo J. A., Trigo-Rodríguez J. M., Borovička J., Tamazian V. S., Fernandes V. A., Llorca J., 2008, *Earth Moon Planets*, 102, 537
- Drummond J. D., 1981, *Icarus*, 45, 545
- Drummond J. D., 1982, *Icarus*, 49, 143
- Dunn T. L., Cressey G., McSween, Harry Y. Jr, McCoy T. J., 2010a, *Meteorit. Planet. Sci.*, 45, 123
- Dunn T. L., McSween, Harry Y. Jr, McCoy T. J., Cressey G., 2010b, *Meteorit. Planet. Sci.*, 45, 135
- Edwards W. N., Hildebrand A. R., 2004, *Meteorit. Planet. Sci.*, 39, 1149
- Edwards W. N., Eaton D. W., Brown P. G., 2008, *Rev. Geophys.*, 46, RG4007
- Egal A., Gural P. S., Vaubaillon J., Colas F., Thuillot W., 2017, *Icarus*, 294, 43
- Ferus M. et al., 2020, *Icarus*, 341, 113670
- Gallardo T., 2006, *Icarus*, 184, 29
- Gardiol D. et al., 2021, *MNRAS*, 501, 1215
- Granvik M. et al., 2018, *Icarus*, 312, 181
- Gritsevich M. I., 2007, *Solar Syst. Res.*, 41, 509
- Gritsevich M. I., 2009, *Adv. Space Res.*, 44, 323
- Gritsevich M. I., Stulov V. P., Turchak L. I., 2012, *Cosmic Res.*, 50, 56
- Grossman J., Rubin A., 2006, White paper report for the nomenclature committee on the composition of olivine and pyroxene in equilibrated ordinary chondrites. Nomenclature Committee, The Meteoritical Society, available at <https://www.lpi.usra.edu/meteor/docs/whitepaper.pdf>
- Gutenberg B., Richter C. F., 1956, *Bull. Seism. Soc. Am.*, 46, 105
- Halliday I., Blackwell A. T., Griffin A. A., 1978, *JRASC*, 72, 15
- Halliday I., Blackwell A. T., Griffin A. A., 1990, *Meteoritics*, 25, 93
- Hildebrand A. R., McCausland P. J. A., Brown P. G., Longstaffe F. J., Russell S. D. J., Tagliaferri E., Wacker J. F., Mazur M. J., 2006, *Meteorit. Planet. Sci.*, 41, 407
- Instituto Geográfico Nacional, 1999, *Spanish Digital Seismic Network*. International Federation of Digital Seismograph Networks, available at <https://www.fdsn.org/networks/detail/ES/>
- Jenniskens P. et al., 2009, *Nature*, 458, 485
- Jenniskens P. et al., 2012, *Science*, 338, 1583
- Jenniskens P. et al., 2014, *Meteorit. Planet. Sci.*, 49, 1388
- Jenniskens P. et al., 2019, *Meteorit. Planet. Sci.*, 54, 699
- Jenniskens P. et al., 2020, *Meteorit. Planet. Sci.*, 55, 535
- Jenniskens P. et al., 2021, *Meteorit. Planet. Sci.*, 56, 844
- Jopek T. J., 1993, *Icarus*, 106, 603
- Kartashova A., Golubaev A., Mozgova A., Chuvashov I., Bolgova G., Glazachev D., Efremov V., 2020, *Planet. Space Sci.*, 193, 105034
- Keay C. S. L., 1992, *Meteoritics*, 27, 144
- Kholshchevnikov K. V., 2008, *Celest. Mech. Dyn. Astr.*, 100, 169
- Kholshchevnikov K. V., Kokhirova G. I., Babadzhanov P. B., Khamroev U. H., 2016, *MNRAS*, 462, 2275
- Kiountouzis E. A., 1973, *J. Roy. Stat. Soc.: Series C (Applied Statistics)*, 22, 69
- Krischer L., Megies T., Barsch R., Beyreuther M., Lecocq T., Caudron C., Wassermann J., 2015, *Comput. Sci. Discov.*, 8, 014003
- Kulichkov S. N., 2004, *Meteorol. Atmospheric Phys.*, 85, 47
- Llorca J. et al., 2005, *Meteorit. Planet. Sci.*, 40, 795
- Llorca J., Gich M., Molins E., 2007, *Meteorit. Planet. Sci.*, 42, A177
- Llorca J. et al., 2009, *Meteorit. Planet. Sci.*, 44, 159
- Madiedo J. M., Trigo-Rodríguez J. M., Alonso J., Zamorano J., Ocaña F., Docobo J. A., Pujols P., Lacruz J., 2009, *EPSC*, 560
- McCrosky R. E., Posen A., Schwartz G., Shao C. Y., 1971, *SAO Special Report 336*, Smithsonian Astrophysical Observatory, Cambridge, MA
- Meier M. M. M., Gritsevich M., Welten K. C., Lyytinen E., Plant A. A., Maden C., Busemann H., 2020, *EPSC Abstracts*, Vol.14, EPSC2020-730
- Milanov D. V., Milanova Y. V., Kholshchevnikov K. V., 2019, *Celest. Mech. Dyn. Astr.*, 131, 5
- Milley E. P., 2010, Master's thesis, Univ. Calgary
- Moilanen J., Gritsevich M., Lyytinen E., 2021, *MNRAS*, 503, 3337
- Morrison S. M. et al., 2018, *American Mineral.*, 103, 848
- Öpik E. J., 1970, *Irish AJ*, 9, 308
- Park R. S., Folkner W. M., Williams J. G., Boggs D. H., 2021, *AJ*, 161, 105
- Passey Q. R., Melosh H. J., 1980, *Icarus*, 42, 211
- Peña-Asensio E., Trigo-Rodríguez J. M., Gritsevich M., Rimola A., 2021, *MNRAS*, 504, 4829
- Popova O., Borovička J., Hartmann W. K., Spurný P., Gnos E., Nemtchinov I., Trigo-Rodríguez J. M., 2011, *Meteorit. Planet. Sci.*, 46, 1525
- Rice J. R., White J. S., 1964, *SIAM Rev.*, 6, 243
- Rochette P., Sagnotti L., Bourot-Denise M., Consolmagno G., Folco L., Gattacceca J., Osete M. L., Pesonen L., 2003, *Meteorit. Planet. Sci.*, 38, 251
- Rubin A. E., 1990, *Geochim. Cosmochim. Acta*, 54, 1217
- Sansom E. K. et al., 2019, *ApJ*, 885, 115
- Sansom E. K. et al., 2020, *Meteorit. Planet. Sci.*, 55, 2157
- Schiaparelli M. J. V., 1867, *Astronom. Nachr.*, 68, 331
- Schultz P. H., Sugita S., 1994, Abstracts of the 25th Lunar and Planet. Sci. Conf., p 1215
- Shober P. M. et al., 2022, *Meteorit. Planet. Sci.*, 57, 1146
- Shoemaker E. M., Helin E. F., Roman B. P., Crockett R., 1989, *IAU Circ.*, 4847, 1
- Shrbený L., Spurný P., Borovička J., 2020, *Planet. Space Sci.*, 187, 104956
- Silber E. A., ReVelle D. O., Brown P. G., Edwards W. N., 2009, *J. Geophys. Res. (Planets)*, 114, E08006
- Silber E. A., Boslough M., Hocking W. K., Gritsevich M., Whitaker R. W., 2018, *Adv. Space Res.*, 62, 489
- Southworth R. B., Hawkins G. S., 1963, *Smithsonian Contrib. Astrophys.*, 7, 261
- Spurný P., Oberst J., Heinlein D., 2003, *Nature*, 423, 151
- Spurný P., Borovička J., Kac J., Kalenda P., Atanackov J., Kladnik G., Heinlein D., Grau T., 2010, *Meteorit. Planet. Sci.*, 45, 1392
- Spurný P., Bland P. A., Shrbený L., Towner M. C., Borovička J., Bevan A. W. R., Vaughan D., 2011, *Meteorit. Planet. Sci. Suppl.*, 74, 5101
- Spurný P. et al., 2012, *Meteorit. Planet. Sci.*, 47, 163
- Spurný P., Haloda J., Borovička J., Shrbený L., Halodová P., 2014, *A&A*, 570, A39
- Spurný P., Borovička J., Haloda J., Shrbený L., Heinlein D., 2016, 79th Annual Meeting of the Meteoritical Society, 6221
- Spurný P., Borovička J., Baumgarten G., Haack H., Heinlein D., Sørensen A. N., 2017, *Planet. Space Sci.*, 143, 192
- Spurný P., Borovička J., Shrbený L., 2020, *Meteorit. Planet. Sci.*, 55, 376
- Steel D. I., Asher D. J., Clube S. V. M., 1991, *MNRAS*, 251, 632
- Stöffler D., Keil K., Scott E. R. D., 1991, *Geochim. Cosmochim. Acta*, 55, 3845
- Storn R., Price K., 1997, *J. Glob. Optim.*, 11, 341
- Stulov V. P., 1997, *Appl. Mech. Rev.*, 50, 671
- Stulov V. P., 2000, *Solar Syst. Res.*, 34, 496
- Tabetah M. E., Melosh H. J., 2018, *Meteorit. Planet. Sci.*, 53, 493
- Trigo-Rodríguez J. M., Borovička J., Spurný P., Ortiz J. L., Docobo J. A., Castro-Tirado A. J., Llorca J., 2006, *Meteorit. Planet. Sci.*, 41, 505
- Trigo-Rodríguez J. M., Borovička J., Llorca J., Madiedo J. M., Zamorano J., Izquierdo J., 2009, *Meteorit. Planet. Sci.*, 44, 175
- Trigo-Rodríguez J. M. et al., 2015, *MNRAS*, 449, 2119
- Unsalan O. et al., 2019, *Meteorit. Planet. Sci.*, 54, 953
- Vida D. et al., 2021, *EPSC Abstracts*, 15, 2021-139
- Vokrouhlický D., Farinella P., 2000, *Nature*, 407, 606
- Whipple F. L., Jacchia L. G., 1957, *Smithsonian Contrib. Astrophys.*, 1, 183
- Wlotzka F., 2005, *Meteorit. Planet. Sci.*, 40, 1673
- Young R. A., 1993, *Introduction to the Rietveld Method*, Vol. 5. Oxford Univ. Press, Oxford, p. 1
- Zuluaga J. I., Cuartas-Restrepo P. A., Ospina J., Sucerquia M., 2019, *MNRAS*, 486, L69

This paper has been typeset from a $\text{\TeX}/\text{\LaTeX}$ file prepared by the author.